SLAC-R-1117

In-situ Data Acquisition and Tool Development for Additive Manufacturing Metal Powder System

Principle Investigators:
32035 - Matthew Kramer, mjkramer@ameslab.gov
32037 - Tony van Burren, vanbuuren1@llnl.gov
32038 - Michael F. Toney, mftoney@slac.stanford.edu

March 31, 2019

SLAC National Accelerator Laboratory, Stanford University, Stanford, CA 94309

This report is based upon work supported by the U. S. Department of Energy under Award No. 32035, 32037, and 32038. Lawrence Livermore National Laboratory is operated by Lawrence Livermore National Security, LLC, for the U.S. Department of Energy, National Nuclear Security Administration under Contract DE-AC52-07NA27344 and Office of Science, DE-AC02-76SF00515. LLNL-AR-770682

Final Technical Report

Project Title: In-situ Data Acquisition and Tool Development for Additive Manufacturing Metal Powder Systems

CPS Agreement Number: 32035, 32037 & 32038

Project Period: 08:2016 – 12:2018

Principle Investigators:

32035, Matthew Kramer, 515-294-0276, mjkramer@ameslab.gov
32037, Tony van Burren, 925-423-5639, vanbuuren1@llnl.gov
32038, Michael F. Toney, 650-926-2056, mftoney@slac.stanford.edu

Authors:

Nick Calta, 925-423-3023, calta1@llnl.gov
Pete Collins, 515-294-5127, pcollins@iastate.edu
Aiden Martin, 925-423-9218, martin248@llnl.gov
Manyalibo Matthews, 925-424-6762, matthews11@llnl.gov
Johanna Nelson Weker, 650-926-5565, jlnelson@slac.stanford.edu
Ryan Ott, 515-294-3616, rtott@ameslab.gov
Kevin Stone, 650-926-7443, khstone@slac.stanford.edu
Christopher Tassone, 650-926-3124, tassone@slac.stanford.edu

Recipient Organizations:

32035, Ames Laboratory, Ames, IA
32037, Lawrence Livermore National Laboratory, Livermore, CA
32038, SLAC National Accelerator Laboratory, Menlo Park, CA

Other project team member organizations: none

Date of Report: March 31, 2019

Acknowledgment, Disclaimer and Proprietary Data Notice –
DOCUMENT AVAILABILITY

Acknowledgment: This report is based upon work supported by the U. S. Department of Energy under Award No. 32035, 32037, and 32038. Lawrence Livermore National Laboratory is operated by Lawrence Livermore National Security, LLC, for the U.S. Department of Energy, National Nuclear Security Administration under Contract DE-AC52-07NA27344 and Office of Science, DE-AC02-76SF00515. LLNL-AR-770682

Table of Contents

List of Acronyms 4

Lists of Figures 5

List of Tables 6

Executive summary 7

Introduction 8

Background 9

Results and Discussion 10

1. Single layer powder bed for *in situ* X-ray characterization 10

2. X-ray imaging of laser powder bed fusion 13

2.1. Identifying Keyhole Regime and Void Formation 14

2.2. Vapor Depression Dynamics 16

2.3. Bubble Dynamics 18

2.4. Turnarounds 21

2.5. Void Repair Strategies 23

3. X-ray diffraction of laser powder bed fusion 24

3.1. Automated data analysis 33

4. Flexible powder feed system for *in situ* X-ray characterization 37

5. Powder characterization at Ames 38

Benefits Assessment 40

Commercialization 40

Accomplishments 41

Conclusions 42

References 42

List of Acronyms

Additive manufacturing (AM)
back scattered electron (BES)
computer-aided design (CAD)
electrode induction gas atomization (EIGA)
energy dispersive spectroscopy (EDS)
heat affected zone (HAZ)
Kolmogorov-Smirnov (KS)
Laser powder bed fusion (LPBF)
Lawrence Livermore National Laboratory (LLNL)
melted zone (MZ)
plasma rotating electrode process (PREP)
SLAC National Accelerator Laboratory (SLAC)
Three dimensional (3D)
Ti-6Al-4V (Ti64)
X-ray diffraction (XRD)

Lists of Figures

Figure 1. Diagram of the experimental geometry. 11
Figure 2. Optical diagnostics added to the LPBF testbed during upgrades at LLNL. 12
Figure 3. Images collected by the melt pool monitoring camera at LLNL. 13
Figure 4. Frequency of void defect formation as a function of laser power. 15
Figure 5. Changing depth and shape of vapor depression moving through the sample. 16
Figure 6. Average depth of voids and vapor depression as a function of laser power. 16
Figure 7. Distribution of void depths at the slower speed for different laser powers. 17
Figure 8. Distribution of void depths at the fast speed for different laser powers. 18
Figure 9. Images of the formation of two voids from one bubble. 19
Figure 10. Snapshots of the recapture of a gas bubble by the vapor depression. 20
Figure 11. Illustration of the experimental geometry for laser turn point experiments. 21
Figure 12. Melt depression depth at turn around point for different laser parameters. 22
Figure 13. Mitigation of voids during laser turn around points by power modulation. 22
Figure 14. Test of the effect of laser power on the success of repairing voids. 24
Figure 15. Example *in situ* diffraction data. 25
Figure 16. *In situ* cooling rates. 27
Figure 17. Surface track widths as a function of laser power. 29
Figure 18. Correlated cooling rates structural parameters and phase fraction changes 31
Figure 19. BSE image of the base substrate far from the heat affected zone. 31
Figure 20. BSE image of the melt pool, heat affected zone (HAZ) and base substrate. 32
Figure 21. Schematic view of diffraction data collection process across the sample. 33
Figure 22. Example of a cluster map for one of the Ti64 cross-sections. 35
Figure 23. Combined cluster analysis on four cross-sections with different laser powers. 36
Figure 24. BSE images for the same four cross-sections in Figure 23. 37
Figure 25. CAD models of flexible multi-layer powder feed system. 38
Figure 26. Oxygen, nitrogen, carbon, and sulfur content in the powders. 39
Figure 27. Flow rates of different powders. 39
Figure 28. SEM of different powders. 40

List of Tables

Table 1. EDS analysis of selected areas from Figure 19 32
Table 2. EDS analysis of selected areas from Figure 20 33

Executive summary

Metal additive manufacturing (AM) is a processing technology which builds 3D components from the bottom-up by selectively melting metal precursors to build a component part in a layer by layer fashion. This advanced manufacturing process promises to initiate a digital renaissance in American manufacturing by decreasing costs, increasing energy efficiency, enabling new component designs, and providing a manufacturing pathway for novel materials which cannot be processed by traditional means. In particular, additively produced parts offer designs that are otherwise impossible to fabricate, custom designs for a single part at no additional cost, and considerable weight savings when compared to conventional production techniques.

In spite of the promising advantages of metal AM, broad adoption of the technology is slow because of fundamental gaps in understanding the link between processing parameters and the properties of the final build. A key gap in this knowledge comes from not being able to access the subsurface dynamics within the metal part during the build. With subsurface characterization models could be rapidly validated and their input parameters tuned with measurable data. This would enable faster qualification of specific builds and an understanding of how the processing conditions should be changed to accommodate modifications in a part design. Finally, with increased understanding of the fundamental laser beam metal interaction we would be able to design novel metal alloys specifically tuned to desired properties such as strength and lightweight. This will open the door to manufacturing parts from the bottom up with the goal of producing the most energy efficient parts for a specific purpose, where the choice of materials can be independent to design choices and both optimized for the use case of the part.

The aim of this project was to develop *in situ* X-ray characterization tools for studying these subsurface dynamics on the relevant length and time scales and connect the observed phenomena to properties in the final builds. It also explored the potential of *in situ* X-ray characterization on multilayer powder bed printing and directed energy powder feed systems. Finally, the project incorporated high speed visible imaging and pyrometry to measure the surface temperature of the melt pool into our *in situ* testbed to enable simulations surface and subsurface characterization during a build.

The project successfully studied keyhole void formation at the base of the laser-formed vapor depression with X-ray imaging over a range of laser scan speeds and powers in the Ti-6Al-4V alloy. We found that on average voids form within a standard deviation of the base of the vapor depression or slightly shallower and the variability in both the vapor depression and void depths increases with increased power and decreased speed. We were able to track the motion of gas/vapor bubbles inside the melt pool and observe both bubble break up and recapture by the vapor depression. We also explored the mechanism behind the clustering of voids at the edge of parts where the laser turns around at the end of a scan line. To avoid this pore formation mechanism, we testing a mitigation strategy, in which we reduced the laser power through the turn point. We were able to verify the improved build quality with the mitigation strategy with *in situ* X-ray imaging.

With *in situ* X-ray diffraction we measured the cooling rates inside the metal after resolidification for different laser powers. We correlated these rates to changes in structural parameters and the phase fraction of room temperature α phase and the higher temperature β phase. We found these differences could be related to compositional changes observed in microstructure seen with scanning electron microscopy on *ex situ* cross-sections of these printed parts.

The success of this project has demonstrated to industry the value in utilizing *in situ* X-ray characterization. The importance of these tools has been acknowledged by the additive manufacturing community with interest in utilizing the tools and/or the data and knowledge

generated by it. However, the current status of commercialization hinges on the demonstration of *in situ* X-ray characterization multilayer and linking more routine surface probes such as high speed visible light imaging and thermal imaging with the synchrotron-based X-ray analysis to enable inline diagnostics without the need of synchrotron radiation.

Introduction

Additive manufacturing (AM) is a promising metal manufacturing technology that promises to increase energy efficiency and decrease costs in both the manufacturing of and the utilization of parts. Moreover, AM can enable new component design motifs and provide a means of developing novel materials which are inaccessible to transitional processing techniques. There are a number of different manufacturing methods under the umbrella of additive manufacturing. This project primarily focused on laser powder bed fusion, where a layer of metal powder is selectively melted with a laser before a fresh layer of powder is added on top.

Currently, a wide range of industries recognize the potential disruptive nature of AM. However, the challenge facing companies wishing to adopt AM processing is that the physical details associated with the process itself are not completely understood. Indeed, the far-from-equilibrium nature of AM processes result in a process space that is very ill-defined by current models and which cannot be simulated using process simulation packages currently adopted by industry. Simply put, the relationships between AM processing parameters and the resulting evolution of composition and microstructure are not well understood as the component geometry and microstructure are dynamically changing during the process resulting in complex, spatially varying thermal histories. These thermal histories, in turn, often lead to spatially varying composition and microstructure and can result in profound differences in the texture, grain structures and defects that will impact the mechanical properties.

While metal AM holds the potential for broad impact across a wide range of industries, current adoption remains limited due to the challenges identified in the previous paragraph. To date, industrial adoption is limited to industries where the immediate impact is more obvious. The most prominent examples include for medical or dental implants because producing bespoke parts for an individual patient is extremely valuable, and in the aerospace industry because of the potential weight savings from AM leads to very significant efficiency gains. The primary obstacle to broader industrial adoption from AM is long qualification lead times and increased uncertainty about materials properties when compared to conventional production because of the relatively underdeveloped understanding of fundamental relationships between process parameters and final mechanical properties of AM parts. The work in this project aimed to accelerate the adoption of additive manufacturing for metallic components across the manufacturing sector by developing sophisticated AM testbed tools to enable rapid process development and informed qualification of the AM components and processes. The testbed we developed allows for small scale testing coupled with otherwise impossible sub-surface X-ray based probes of the material during the AM process. We engaged with industry stakeholders to ensure that our test bed capabilities and experimental campaigns, such as comprehensive process monitoring and quality control, align well with industry needs. We determined that based on assessments of data collected under this project, the testbed can provide valuable data to industrial stakeholders and enable accelerated AM adoption by identifying process conditions that produce unwanted pore defects and directly validate mitigation strategies targeted at eliminating pore formation. Future work should focus on linking the subsurface X-ray characterization to more routine optical surface probes to enable

inline diagnostics without the need of synchrotron radiation. Additionally, the capability of *in situ* X-ray characterization of multilayer builds, which was not within the scope of this project, is needed to decrease risk and increase commercial interest.

Background

When this work started, the state of the art in the field related exclusively to *in situ* X-ray experiments on laser welding, using both imaging and diffraction, as well as *in situ* optical imaging. Since then various other groups in addition to this project team have begun work on *in situ* X-ray measurements to study laser powder bed fusion (LPBF).

High-speed visible imaging is a powerful tool to probe the evolution of melt pool morphology and powder movement in and around the melt pool during a build.[1–3] For example, Ly *et al*. resolved the origins of hot droplet ejection or spatter emanating from the melt pool region during LPBF.[2] Bidare *et al.* used Schlieren imaging to understand the interaction of the laser plume with process gas in the build chamber.[4,5] In addition to visible light-illuminated imaging, thermal emission imaging has been used to measure the surface temperature of the melt pool [6–9] or entire build.[10] Melt pool morphology has also been investigated via in situ measurements of the pool depth using inline coherent imaging, an interferometry-based technique.[11] While these approaches based on optical methods provide important information about the dynamics of the LPBF process, they are limited to surface imaging only and cannot provide information about bulk material behavior. In contrast, X-ray-based probes are highly penetrating and can non-destructively capture melt pool dynamics in the bulk as well as provide structural information through diffraction. Taken together, high speed optical, thermal, and X-ray diagnostics can provide highly complementary information about process dynamics during LPBF.

Many of the rapid solidification phenomena relevant to LPBF are similar to those present in welding. Elmer and coworkers carried out numerous X-ray diffraction experiments during welding and quantified the dynamics of solidification and solid state phase transitions on cooling for Ti alloys[12–14] and stainless steels.[15–17] Yonemura *et al*. also used time-resolved synchrotron X-ray diffraction to study the dynamics of solidification during welding of stainless steel.[18] While this prior work provides important context for understanding solidification and phase transitions in LPBF, the time scales relevant for welding are much longer than the dynamics of LPBF. Time resolution of 100 ms is sufficient to resolve cooling dynamics in diffraction experiments of Ti-6Al-4V (Ti-64) welding,[12] while cooling in LPBF is expected to occur on time scales of a few milliseconds.[19] Therefore, higher sampling rates are required to completely elucidate the dynamics of the laser-material interaction in LPBF. Zhao *et al.* have reported high-speed X-ray imaging and diffraction of the interaction between a laser and Ti-64 powder under spot melting conditions similar to LPBF.[20] Additional work by the same group have expanded their approach at the Advanced Photon Source (at Argonne National Laboratory) to look at scanned beams[21] and have focused on assessing the geometry of the keyhole under a wide variety of laser scan speed and power conditions for Ti-6Al-4V.[22] Kenel *et al*. performed in situ X-ray microdiffraction of rapid solidification in Ti-64 under well-defined cooling conditions with 1 ms time resolution, providing additional insight into the fundamental solidification behavior of this alloy under LPBF-like conditions.[23] They performed cyclic heating and cooling to elucidate microstructural evolution induced by thermal behavior similar to what occurs in a multi-layer build, though the thermal boundary conditions in their experiment represent a somewhat different case than what is present in an LPBF build.

The team combined expertise from Lawrence Livermore National Laboratory (LLNL), SLAC National Accelerator Laboratory (SLAC), and Ames Laboratory. Key team members at LLNL include Tony Van Buuren, the deputy division leader of the materials science division and an expert in X-ray science and has over twenty years' experience in materials characterization using X-ray based diagnostics; Manyalibo (Ibo) Matthews, the group leader of the laser materials interaction science group and an expert in laser-materials processing techniques including metal AM; Nicholas Calta, a staff scientist in the materials science division with expertise in *in situ* and *ex situ* characterization of metal AM using both optical and X-ray based probes; and Aiden Martin, a staff scientist in the materials science division with expertise in using *in situ* diagnostics to understand laser and electron-beam materials processing techniques. The team at SLAC includes Christopher Tassone, a staff scientist in the materials science division with extensive expertise developing *in situ* X-ray scattering approaches to understanding material formation processes; Johanna Nelson Weker, a staff scientist in the materials science division with extensive experience in *in situ* X-ray microscopy studies of various materials systems; Kevin Stone, a staff scientist in the materials science division and an expert in extracting detailed crystallographic and microstructural information from X-ray diffraction data; and Michael Toney, a distinguished staff scientist and head of the SSRL materials science division who is a world leader in X-ray based characterization of energy materials with three decades of experience using X-ray techniques for materials characterization. The team at Ames lab includes Matt Kramer, a senior scientist and adjunct professor of materials science and engineering at Iowa State who is an expert in using X-ray diffraction to study phase transformations *in situ*; Ryan Ott, a staff scientist at Ames laboratory with expertise in *in situ* synchrotron X-ray studies of phase transformations and deformation behavior in metals and alloys; and Peter Collins, a group leader at Ames Laboratory who is an expert in physical metallurgy of non-ferrous alloys, particularly Ti-based alloys.

Results and Discussion

1. Single layer powder bed for *in situ* X-ray characterization

To facilitate the *in situ* X-ray imaging and diffraction experiments during laser powder bed fusion (LPBF) planned under this project, it was necessary to design and build a testbed LPBF instrument compatible with operation at a synchrotron X-ray facility. Design, assembly, and initial experiments were completed in the first year of the project and are described in a publication by Calta *et al*..[24] A schematic representation of the experimental geometry is shown in Figure 1.

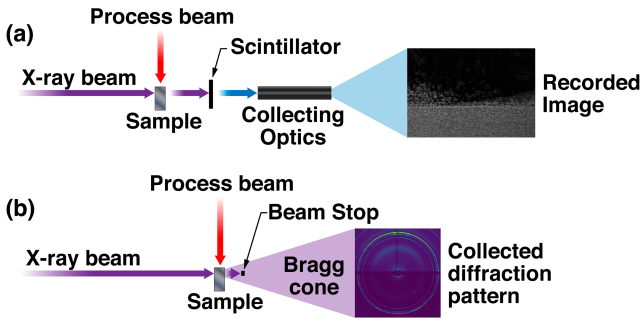

Figure 1. Diagram of the experimental geometry. (a) Experimental imaging setup, illustrating that the X-ray beam impinges on the sample, then hits a scintillator to be converted to visible light. This visible light is imaged onto a high speed camera. (b) Illustrates the diffraction setup, in which the X-ray beam hits the sample and scattered X-rays are directly detected by a hybrid photon counting detector positioned behind the sample.

The instrument is designed to faithfully replicate a single layer scan of the LPBF process with minimal changes to thermal conditions and other important environmental effects. It uses a 1070 nm continuous wave fiber laser coupled to a 3-axis scan mirror system, analogous to those used in commercial LPBF machines. This process laser is focused to a ~ 50 µm diameter ($D4\sigma$) Gaussian spot and scans across a thin substrate that is contained in a vacuum chamber filled with an Ar environment to avoid oxidation during laser melting. The sample used for most experiments was a ~500 µm thick piece of Ti-6Al-4V as a substrate, in some cases with a ~50-80 µm thick powder layer spread on top of the substrate and in other cases with no powder. The substrate plate was sandwiched between two glassy carbon windows, which serve to confine the powder layer and are X-ray transparent. This sample geometry is thinner than would usually be used in a full scale LPBF build. To ensure that this geometric change did not produce significant unwanted process changes due to the difference in thermal boundary conditions enforced by the geometry, we carried out finite element thermal modelling to understand the effect of boundary conditions on thermal history. These simulations indicate that the sample geometry does not cause a significant change in the thermal conditions in and around the melt pool for a single layer of Ti-64.

The X-ray imaging experiments used beamline 2-2 at the Stanford Synchrotron Radiation Lightsource (SSRL) using polychromatic X-ray radiation. Over the course of the project various detection systems were used in an effort to find an optimal compromise between sampling rate and spatial resolution. The optimal conditions used an unfiltered X-ray spectrum, which passed through the sample to form the image. The X-rays then exit the sample chamber and are converted to visible light by scintillator crystal. The light from the scintillator is directed out of the X-ray beam by a silver-coated mirror and collected by a Mitutoyo 10× /NA0.22 long working distance objective lens. The light is then imaged onto a Photron SA-X2 high speed camera by a tube lens. This detection system provides 2 µm per pixel effective pixel size with sufficient X-ray flux to collect data with a 1024 × 672-pixel field of view at 20 kHz using an exposure time of 25 µs for substrates of Ti or Al alloys.

X-ray diffraction experiments were performed at beamline 10-2 at SSRL using 20 keV monochromatic, focused X-rays. The X-ray beam size was defined by slits and varied throughout

the course of the project depending and ranged from 50 × 50 µm at the smallest to 70 × 350 µm at the largest. The diffraction patterns were collected using an Eiger 1M area detector, which yielded full azimuthal coverage for data with Q_{max} = ~3 Å^{-1} with a Q resolution $\Delta Q/Q$ ~ 0.005 Å^{-1}. Data collection rates necessary to obtain acceptable signal to noise for Ti-based alloys were 1 kHz and 3 kHz for Al alloys.

In the last quarter of the project the AM testbed system was returned to LLNL for refurbishment and significant upgrades, specifically the incorporation of at least one optical process monitor comparable to what is typically included in full scale commercial laser powder bed fusion machines. We selected two process monitors for these upgrades: a high-speed camera and point pyrometer. These monitors were selected because they are commonly available on commercial LPBF machines and both measure thermal emission from the melt pool, which likely correlates with the melt pool dynamics and pore formation we have successfully observed in X-ray imaging. The arrangement of these two diagnostics relative to our process laser is shown in Figure 2.

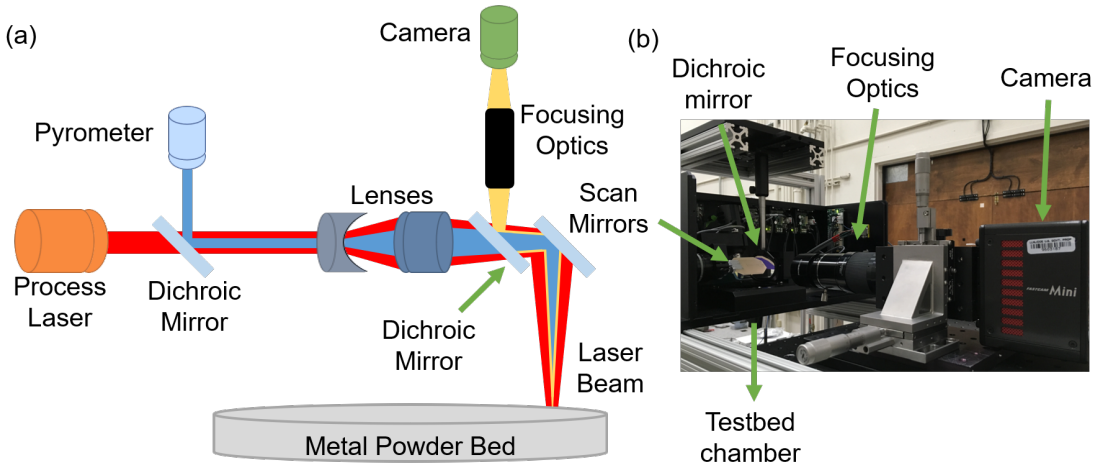

Figure 2. Optical diagnostics added to the LPBF testbed during upgrades at LLNL. (a) Cartoon layout of the optical path, illustrating the location of the pyrometer and monitoring camera. (b) Image of camera, focusing optics, and dichroic mirror used to pick off melt pool image for monitoring. The pyrometer, process laser input, and testbed chamber are not visible from this viewing angle.

Both the pyrometer and camera are capable of high data rate process monitoring, similar to what is available on most full scale LPBF machines. The pyrometer monitors the melt pool at a rate of 100 kHz while the camera operates at ~ 10 kHz, consistent with most melt pool monitoring cameras. By using the scan mirrors that steer the laser as the first optics in the light collection path for both the monitoring camera and the point pyrometer, we ensure that the melt pool is always in the center of the camera field of view and the pyrometer only collects light emitted from the melt pool, which simplifies data analysis and is very similar to monitoring systems that come standard on most modern LPBF machines. Images collected during the first test of the monitoring camera with laser scanning are shown in Figure 3. These data were collected at a frame rate of 6.4 kHz, although the camera is capable of data collection at significantly higher frame rates at these resolutions. The images are cropped to 256 x 256 to make them comparable to data collected by commercial melt pool monitoring cameras. The camera resolves thermal emission from spatter events, fluctuations in the melt pool itself, the vapor plume, and the solidified track as it cools.

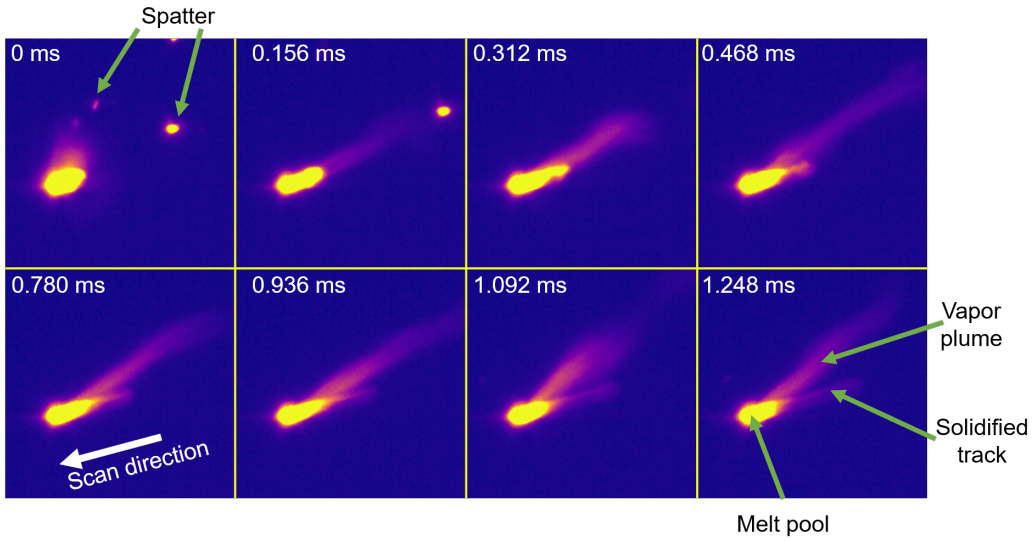

Figure 3. Images collected by the melt pool monitoring camera at LLNL. This test was conducted on a 316L stainless steel bare plate at a frame rate of 6.4 kHz, a scan speed of 800 mm/s, and a laser power of 330 W with the scan direction indicated. Spatial resolution is approximately 10 µm with a field of view of ~2.5 mm. Features corresponding to thermal emission from the melt pool itself, spatter, the vapor plume, and the solidified track are evident.

2. X-ray imaging of laser powder bed fusion

We used high-speed X-ray imaging to probe subsurface melt pool dynamics and void formation mechanisms inaccessible to other monitoring approaches. The ability to image subsurface phenomena allows rapid experimental validation of the calculated keyhole threshold, the threshold at which the metal vaporizes and exerts a force on the molten material, across a large portion of the multidimensional laser parameters. With this technique, we are able to observe vapor bubble formation and motion due to melt pool currents, including instances of bubbles splitting before solidification into clusters of smaller voids while the material rapidly cools and bubbles being recaptured by the vapor depression resulting in no voids in the final part. Such events severely complicate attempts to identify defect formation using surface-sensitive process

monitoring tools. We have explored the different void mitigation strategies for a laser turn around point, a typical scan pattern for the edge of a part. Finally, we studied whether or not a second laser pass could be a viable approach for repairing voids.

2.1. Identifying Keyhole Regime and Void Formation

By adjusting the laser power at two different speeds (146 mm s^{-1} and 455 mm s^{-1}), we compare the frequency of voids as the laser power is increased into the keyhole regime (Figure 4). For the 146 mm s^{-1} laser speed tracks, two different runs for each laser power are averaged together. The error bars show one standard deviation from the average. The onset of void formation for both speeds is around 75 W. Previous studies have predicted that the transition from the conduction regime to keyhole regime occurs when the normalized enthalpy exceeds a value of ~6, while experiments in stainless steel show this transition occurring closer to a normalized enthalpy of ~30.[25,26] Normalized enthalpy ($\Delta H/h_s$) can be written as

$$\frac{\Delta H}{h_s} = \frac{AP}{\pi \rho C T_m \sqrt{Dua^3}} \quad (1)$$

where ΔH is the specific enthalpy, h_s is the enthalpy at melting, A is the absorptivity of the material (assumed here to be 0.6 under all conditions), P is the laser power, ρ is the density (4.43 g cm^{-3} for Ti64),[27] C is the specific heat capacity (0.83 J $g^{-1}K^{-1}$),[27] T_m is the melting temperature (1923 K),[27] D is thermal diffusivity of the melt (0.086 cm^2 s^{-1}),[27] u is the scan speed of the laser, and a is the radius of the laser beam such that $a = \sigma\sqrt{2}$. Normalized enthalpy has been shown to accurately describe the transition from conduction to keyhole regime under different laser scan speeds, power, and beam size.[26] For the two laser scan speeds presented here, the onset of void formation occurs at around a normalized enthalpy of 17 ± 8. This agrees well with the previous experimental estimate (30 ± 4) made on 316L stainless steel using two different beam sizes strengthening the proposition that the normalized enthalpy is indeed a useful metric to compare selective laser melting under varying laser conditions and even across different materials.

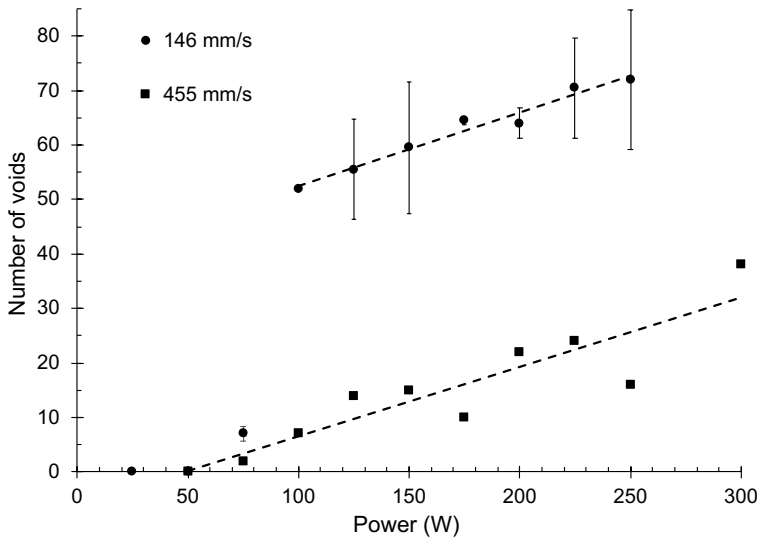

Figure 4. The frequency of void defect formation as the laser power is increased into the keyhole regime for two different laser scan speeds. The faster scan speed shows a linear increase in voids with increased laser power with a slope of 0.1 W^{-1}. The slow speed shows the same linear dependence after a dramatic increase in void formation between 75 and 100 W. The slower scan speed is the average number of voids for two different tracks with the error bars showing one standard deviation.

Immediately after the onset of void formation, the two laser scan speeds behave very differently. We observe that the liquid-vapor interface is more stable at higher scan speeds and is therefore less likely to produce bubbles. The faster scan rate (455 mm s^{-1}) shows a linear increase in the number of voids with increasing power with a slope of 0.1 W^{-1}. However, the slower scan speed (146 mm s^{-1}) shows a sharp jump in the number of voids formed at 100 W before a linear increase with a slope equal to that of the faster scan rate; namely 0.1 W^{-1}. Conversely, well into the keyhole regime where the number of voids form changes linearly at a rate independent of scan speed, the total number of voids is scan speed dependent. These observations suggest that the change in the rate of void formation well into the keyhole regime is adequately described with the laser scan parameters; yet, the void formation mechanism immediately after the onset of void formation cannot be fully explained.

2.2. Vapor Depression Dynamics

From the high-speed *in situ* imaging data, we can also track the vapor depression dynamics formed by the recoil pressure of the vaporized metal as the laser scans across the powder (Figure 5a). The vapor depression shape and depth are highly variable even as the laser is scanned at a constant speed. Dramatic changes in shape and depth of the vapor depression often result in the formation of a vapor-filled bubble forming near the base of the depression. We have tracked the variability in the vapor depression depth as a function of time (Figure 5b) and found an average depth of 262 µm with a standard deviation of 26 µm for a scan speed of 146 mm s^{-1} and laser power of 100 W.

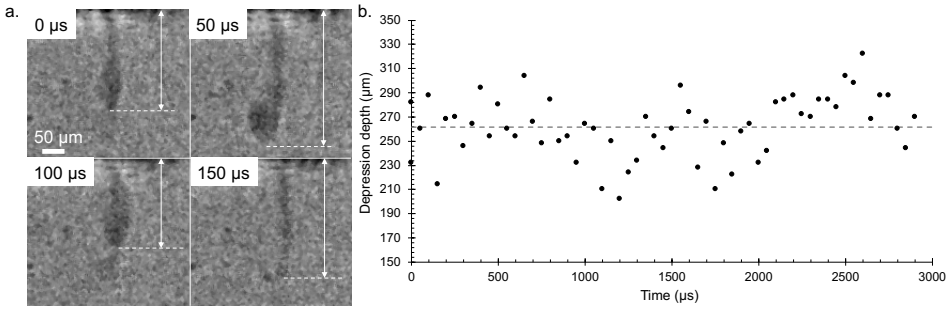

Figure 5. A series of images shows the vapor depression moving through the sample (a). The depth and shape of the vapor depression varies considerably in these four images. The vapor depression depth can be tracked during a scan to see the variation (b). This scan at 146 mm s^{-1} and 100 W shows an average vapor depression depth of 262 µm.

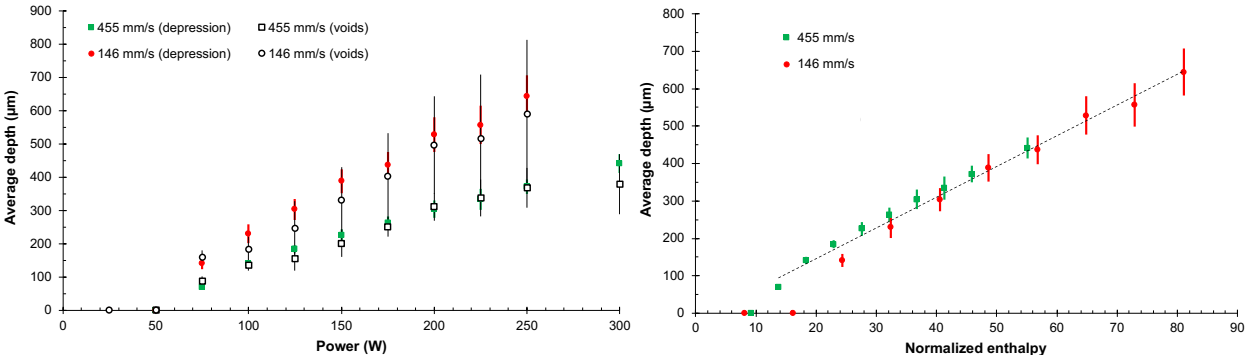

Figure 6. (left) The average depth of the voids with increasing laser power tracks the average vapor depression depth for both 455 mm s^{-1} and 146 mm s^{-1} laser scan speed. On average voids form within a standard deviation (error bars) of the base of the vapor depression or slightly shallower. The variability in both the vapor depression and void depths increases with increased power and decreased speed. (right) Average vapor depression depth is linear with normalized enthalpy.

To better understand the relationship between the vapor depression and void formation we plotted the average vapor depression depth and average void depth as functions of power (Figure 6, left). For both speeds, below a laser powder of 75 W a vapor depression was not visible and void defects do not form. The onset of void formation is also the scan speed and power at which a vapor depression is visible. As the power increases, the depth of both the voids and vapor

depression increase. Moreover, the slower scan speed results in a higher average depth of both voids and the depression for all laser powers investigated.

On average, voids form within a standard deviation (colored error bars) of the base of the vapor depression, and typically slightly shallower. This suggests that voids form when the base of the depression is pinched off as a gas bubble, and the bubbles are not dragged significantly closer to the surface or deeper by the melt pool currents before solidifying. This agrees with what we observe by eye from the X-ray movies of the different prints. Moreover, the spread in the void depth increases considerably with higher power and slower speed as seen in the large standard deviation in the average void depth (black error bars). This large distribution agrees with our observations from the X-ray movies where we find that voids tend to form when the vapor depression depth is near an extreme, either much shallower or deeper than the average depth. Looking closer at the distribution of void depths (Figures 7 and 8) it is difficult to extract a clear trend; nevertheless, it clearly does not resemble a normal distribution centered around the average vapor depression depth.

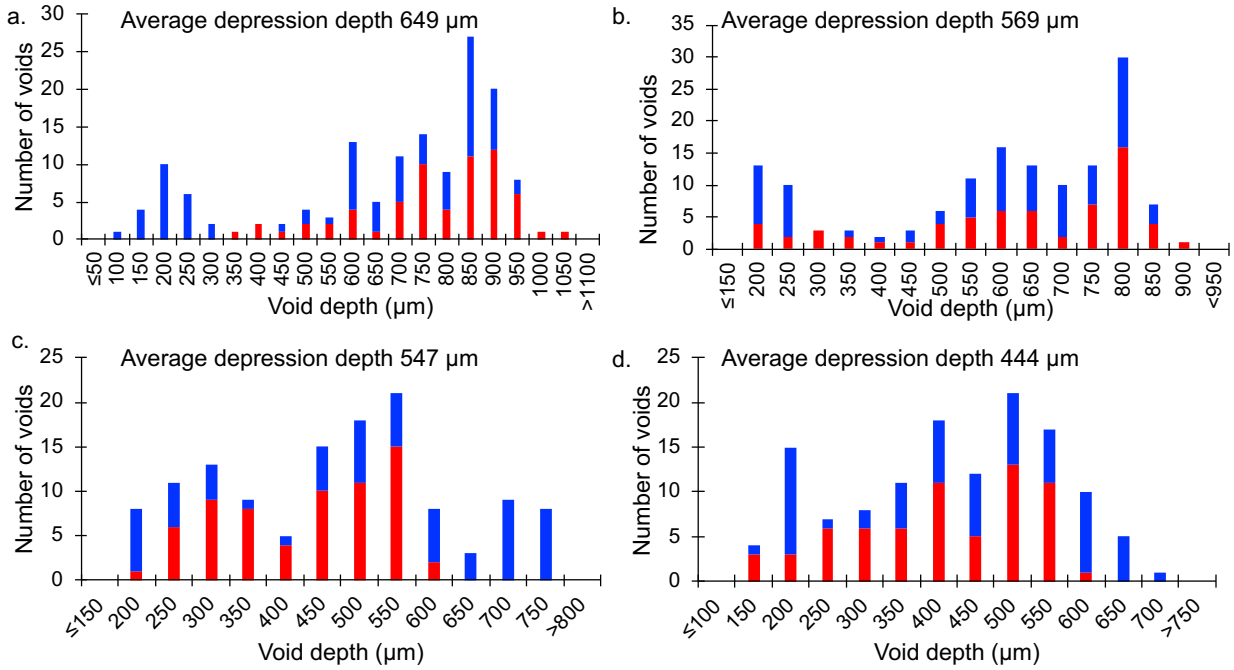

Figure 7. Distribution of void depth for laser scan speed 146 mm s^{-1} for laser powers of a. 250 W, b. 225 W, c. 200 W, and d. 175 W. The two colors indicate the voids from two different tracks.

It is also notable that the average vapor depression depth (and therefore, void depth) is linear with normalized enthalpy for both speeds (Figure 6, right) in the keyhole regime. Thus, normalized enthalpy appears to capture the key mechanisms for the average depth of the vapor depression and resulting voids, but does not accurately predict the number of voids formed for a given set of scan parameters. This could possibly be explained by the fact that the likelihood of void formation is not determined by the normalized enthalpy (or normalized energy density) of the system, but rather the instability of the depression shape and melt pool dynamics. Next, we explore a few observed phenomena related to the dynamics of the melt-vapor interface.

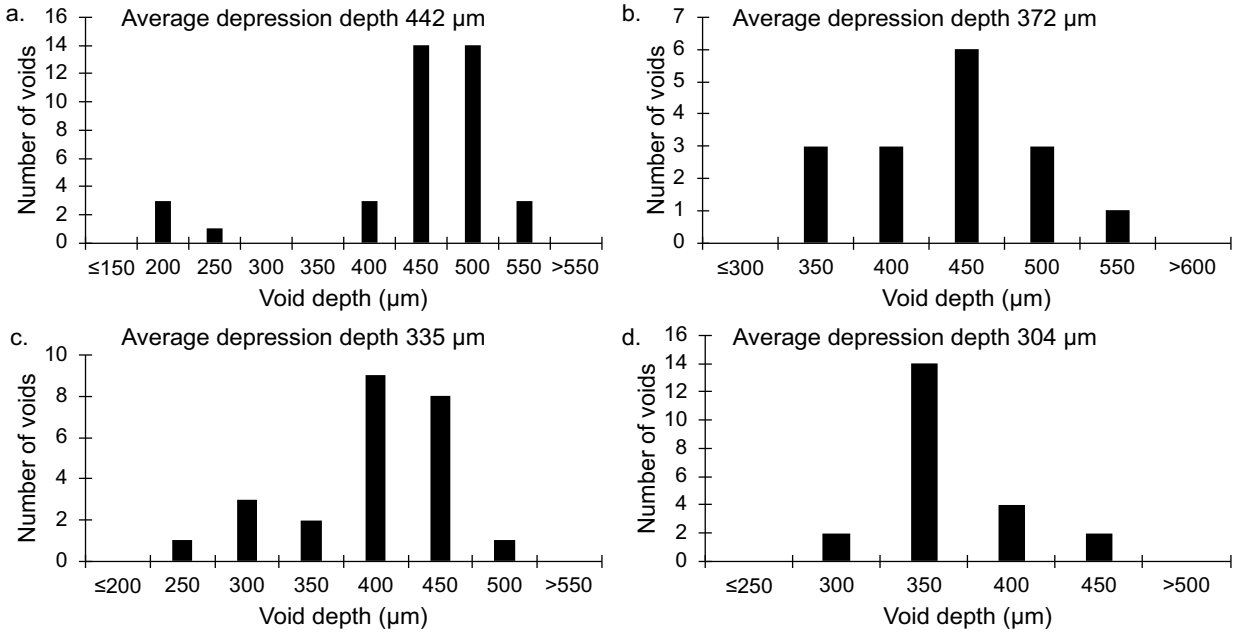

Figure 8. Distribution of void depth for laser speed 455 mm s^{-1} for laser powers of a. 300 W, b. 250 W, c. 225 W, and d. 200 W.

2.3. Bubble Dynamics

In addition to vapor depression dynamics, *in situ* X-ray imaging reveals the dynamic behavior of vapor-filled bubbles as they move through the melt pool and are trapped by solidifying metal. Many of the observed voids appear as expected, developing from the instability of the liquid-vapor interface and solidifying soon after creation. However, we do observe some more interesting, frequent phenomena that should be considered. For example, we frequently observe the breaking apart of single bubbles into two or more bubbles during solidification. An example is shown in Figure 9. In the first panel, the bottom of the vapor depression is slightly bulged suggesting a bubble may form. In the second panel of Figure 9, the bubble is first observed approximately 100 µm behind the depression as the laser scans from left to right. The "x" in each frame indicates the position of the bubble in the second frame. Notably, the bubble appears well past the depression, which only moves ~6 µm between frames. This indicates that the melt pool current for this scan is much faster than we can accurately capture with the camera frame rate used (20 kHz). However, we observe for higher energy density scans, the motion of bubbles in the melt pool is much slower and is captured. Often those bubbles are observed being dragged along by the laser near the surface of the melt pool at depths around 60 – 100 µm and as far as ~300 µm behind the vapor depression.

Based on the imaging, the bubble in Figure 9 travels at 2 m s^{-1} opposite the direction of the laser scan immediately after pinching off the vapor depression, and subsequently decelerates significantly to much slower velocities as it is influenced by the viscosity and currents of the melt pool. By 50 µs after first captured, the bubble splits in two with the higher bubble moving up and away from the vapor depression due to the fluid flow of the melt pool. By 100 µs after formation, both bubbles are trapped as void defects. The behavior of the bubbles primarily depends on the complex fluid flow present in the melt pool and cannot be imaged directly using our setup.

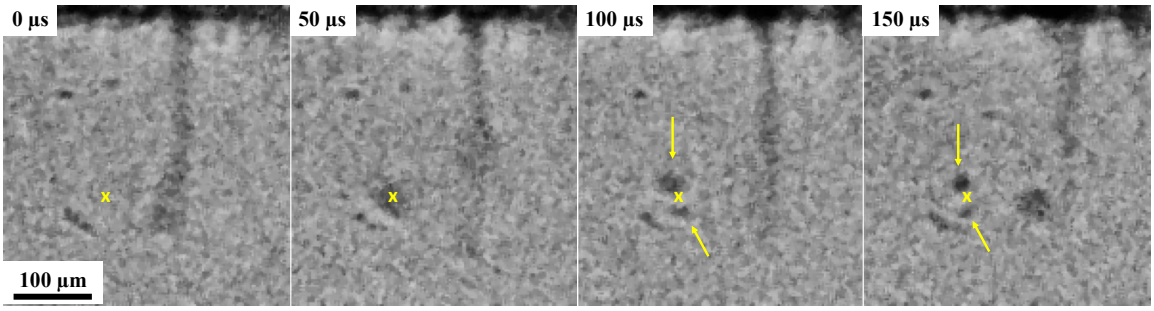

Figure 9. Four consecutive images of the vapor depression showing the formation of two voids from one bubble. As the laser and vapor depression moves from left to right, the void develops after the laser has passed, as seen in the second frame. An "x" is used to mark the location of the void in that second frame. As the laser moves right and the melt pool begins to cool, the void is seen splitting into two voids and solidifying (arrows). The scan was performed at 146 mm s^{-1} and 100 W.

We have found that bubble breakup is a relatively common occurrence for the processing parameters that we examined. In fact, nearly all of the scans with laser power above 100 W for a scan speed of 455 mm s^{-1} and above 75 W for a scan speed of 146 mm s^{-1} show bubble breakup. Since the bubbles tend to form near the bottom of the vapor depression, their formation occurs close in proximity to the edge of the melt pool solid-liquid interface. As a bubble is carried by convective currents away from the vapor depression and depending on the direction of the current, the bottom of the bubble approaches that solid-liquid interface, and the bubble becomes pinned to that location. Marangoni-driven melt pool flow pulls on the top of the bubble and eventually overcomes surface tension to split the bubble.

A second notable bubble dynamic is the recapturing of a bubble by the vapor depression (Figure 10). In this particular case, instability in the vapor depression shape and size leads to a bubble which exists for approximately 100 µs before being recaptured by the depression. The bubble is formed near the vapor depression, creating a situation where it would more likely be recaptured. This self-healing, recapturing event is less frequent than bubbles breaking apart, but also occurs more often in scans with laser power above 100 W for a scan speed of 455 mm s^{-1} and above 75 W for a scan speed of 146 mm s^{-1} where the vapor depression shape is rapidly changing. Bubble recapture and bubble break up are important phenomenon that need careful consideration when developing process monitoring tools which might detect bubble recapture as a void

formation event and give a false positive or bubble break up as only one void rather than a cluster of smaller ones.

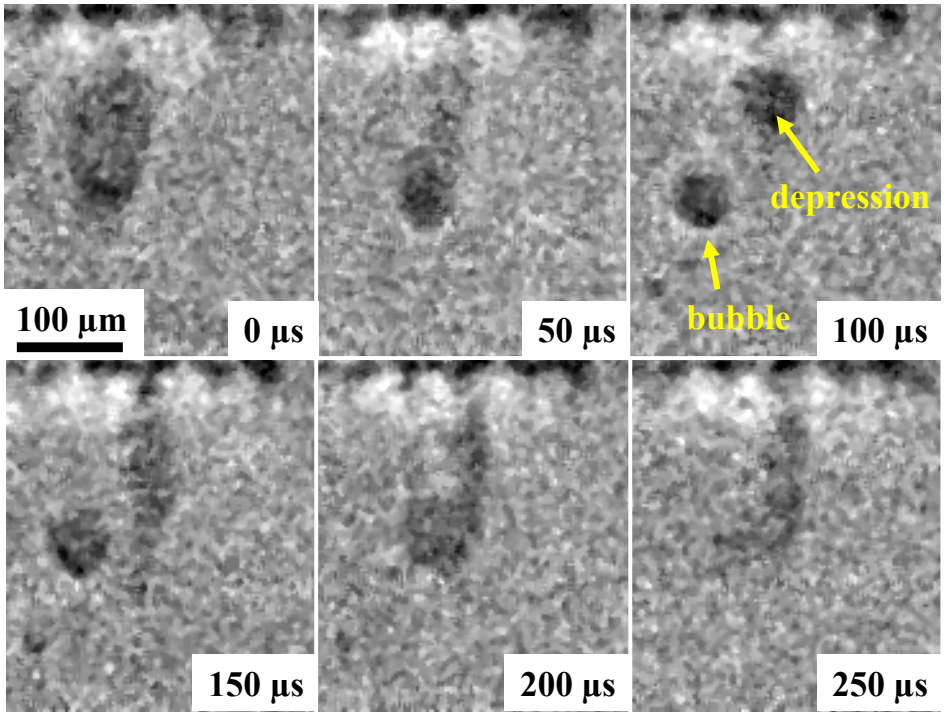

Figure 10. Snapshots showing the recapture of a gas bubble by the vapor depression. The bubble disconnects from the vapor depression after 100 µs. Before the bubble can be solidified into a void, it rejoins the highly unstable vapor depression at 200 µs. Identifying bubble formation before solidification can create false positives for detecting a void formation events by a process monitoring tool. Image was despeckled with ImageJ to remove some noise.

2.4. Turnarounds

In addition to investigating melt pool dynamics and pore formation mechanisms under steady state scanning conditions, we also investigated what occurs during laser turnaround points, which frequently occur near the edges of parts. Previous reports[28] and modelling results indicate that these locations are more likely to cause void formation than bulk regions, even in parts where good processing conditions have been found. This is likely due to the changes in thermal boundary conditions enforced by the laser turning around relative to a normal linear scan. We used *in situ* X-ray imaging to observe the dynamics of pore formation at the turn point, design a mitigation strategy to reduce the likelihood of the pore formation mechanisms we observed, and assess the effectiveness of the mitigation strategy we attempted. The geometry of our turnaround experiments is illustrated in Figure 11.

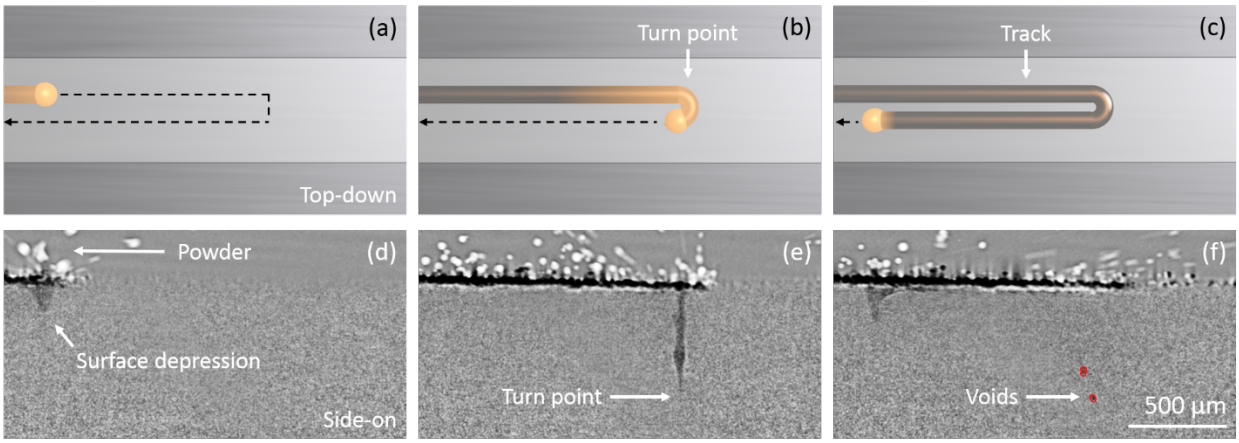

Figure 11. Illustration of the experimental geometry for laser turn point experiments. (a-c) Illustration of the laser turnaround point studied here. (d-f) Time difference X-ray images of a turnaround in Ti-6Al-4V performed at a laser power of 200 W and set scan speed of 1000 mm/s. (d) The laser is scanning from the left to right with spatter and powder above a melt depression due to vapor recoil below. (e) The laser enters the turn point region and the vapor depression digs deep into the substrate. (f) The laser is moving right to left after the turnaround. Keyhole voids at the turnaround location are highlighted in red.

Analysis of imaging data at turn around points illustrate that fundamental properties of the scan mirrors themselves, rather than any programmed laser scan speed, dominate pore formation at turn around points. These experimental observations agree with predictions made by LLNL modelers regarding melt pool behavior at turn around points. The data indicate that at the turn point, the set scan speed has no impact on the melt pool depth or pore dynamics (Figure 12). Instead, these behaviors depend entirely on laser power, because the mirror deceleration and acceleration near the turn point does not depend on the mirror settings, but rather the inertia of the mirrors and scan actuators. Furthermore, this behavior does not substantially differ in cases with powder or with a bare plate substrate.

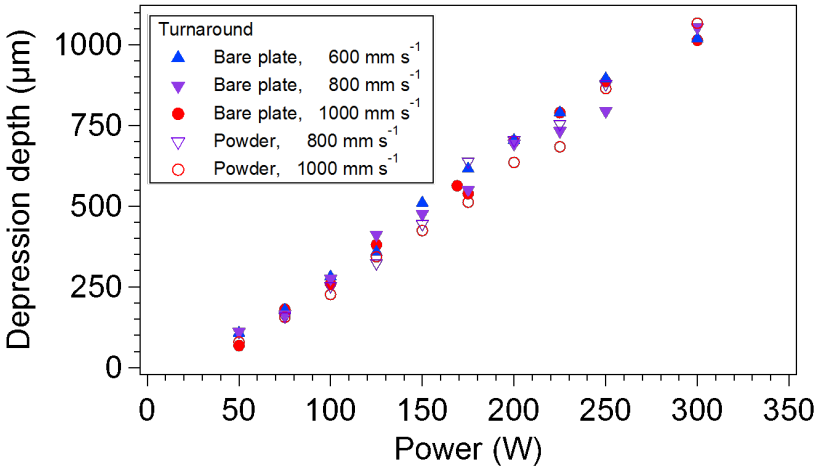

Figure 12. Melt depression depth at the turn around point for a variety of laser powers and scan speeds.

The result of these combined effects causes pores to form at the turn point because of a momentary increase in energy density, in which the constant laser power and effectively slower scan speed push the system into keyhole mode melting. As the mirrors accelerate away from the turn point, the material returns to steady state conduction mode melting, but pores pinch off from the vapor depression during this transition. In order to avoid this pore formation mechanism, we implemented a mitigation strategy, in which we reduced the laser power near the turn point. A schematic of the strategy and differences in pore formation are illustrated in Figure 13. The mitigation strategy shown here shows significant agreement with Multiphysics modeling carried

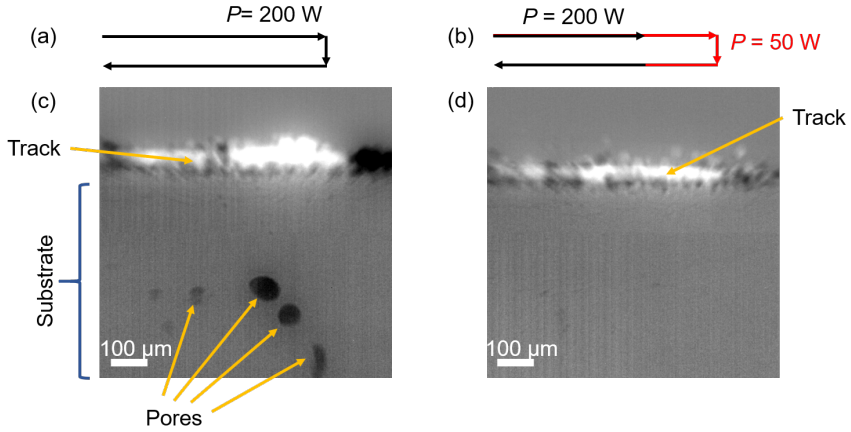

Figure 13. Mitigation of pore formation in Ti64 during laser turn around points by power modulation. (a) A cartoon of the scan strategy used in panel (c), similar to what is used in Figure 1. The scan speed used in this example is 1200 mm/s. (b) A cartoon of the scan strategy used in panel (d), with a reduced laser power at the turn around point. The cartoons in panel (a) and (b) are not to scale. (c) and (d) illustrate the change in density due to the turnaround scans shown in panels (a) and (b), where bright spots represent added material and dark spots represent removed material. Both panels have a clear region of powder removal and melt track added near the top of the sample, while deeper in the substrate (c) contains many large pores while (d) does not.

out in a parallel effort at LLNL, which suggests that this type of laser power modulation can be used as an effective approach to mitigate defect formation mechanisms caused by transient changes in the effective scan speed. These results are described in detail in a publication by Martin *et al*.[29]

2.5. Void Repair Strategies

While determining the controlling mechanisms of void formation in AM processes is critical to advancing AM technologies, equally important is understanding how such defects can be removed or fixed after creation. It has been proposed that scanning the laser over an already printed region can be an effective means of repairing voids.[30] Nondestructive X-ray imaging provides an ideal approach to investigate this strategy for void repair as it allows imaging between multiple laser passes to assess the formation and repair of voids. Here we directly investigated the effectiveness of using a second laser scan with variable laser power to repair keyhole void defects. Prior to laser exposure, no voids are discernable in the substrate. As expected from the work described above, voids result from an initial laser pass with speed of 144 mm s^{-1} and power at 100 W. In an attempt to repair these voids, a second laser pass was executed at 100 W, 150 W, and 50 W using the same scan speed. Images after these passes are shown in Figure 14 where the voids created by the initial scan are colored red if they are successfully repaired by the subsequent scan or magenta if they remain after the repair attempt. New voids formed in the second scan are blue. During the second laser pass at 100 W (Figure 14a), the average vapor depression reaches the same depth within the substrate as the first pass. Thus, the melt pool is around the same depth, melting the same material as the first pass and repairing the voids formed during the original laser scan. However, the second laser scan also forms new voids at approximately the same depth, but in different locations. This suggests that void formation under these conditions primarily arises from the stochastic behavior of melt pool dynamics rather than any preexisting defect in the material itself. This void repair and reformation behavior was consistent over three tracks treated with the same scanning and rescanning strategy. Based on these laser parameters, using a second laser scan with the same laser power does not represent a successful repair strategy for keyhole voids.

When the laser power in the second pass is increased from 100 W to 150 W (Figure 14b), the melt pool extends deeper in the substrate, melting the material around the voids generated during the first pass and repairing them. However, the higher power scan also leaves behind voids deeper into the substrate, between 180 and 385 µm below the surface, consistent with the average void depth results shown in Figure 6. Since the voids are generated on average 50-100 µm shallower than the depth of the vapor depression, a laser pass with a lower laser power may be able to repair the initial voids and form voids higher in the substrate or not form voids at all. To investigate this, a final repair attempt used a second a laser power of only 50 W (Figure 14c). The low power repair track produced a vapor depression that only penetrates roughly 80 µm into the substrate and does not produce any new voids; however, the melt pool does not penetrate deep enough to remove any of the voids formed in the first pass.

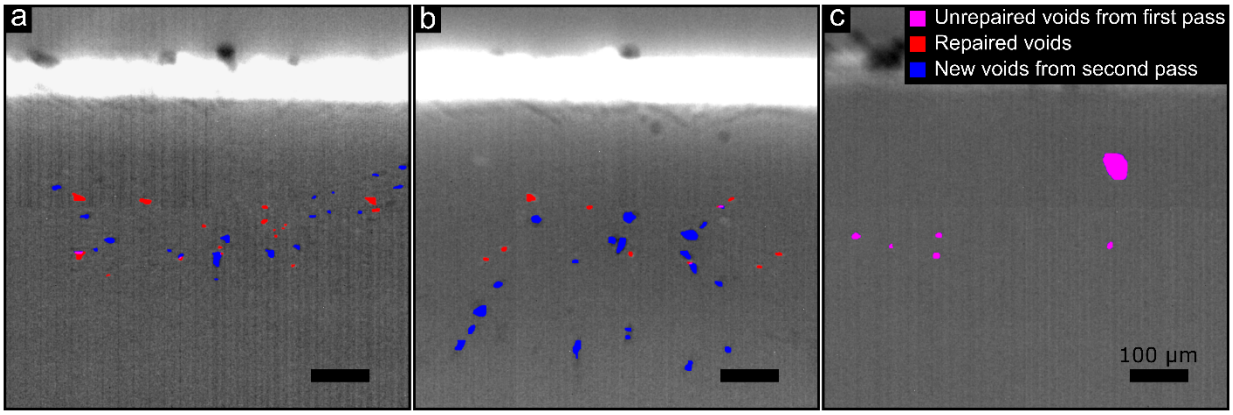

Figure 14. Test of the effect of laser power on the success of repairing voids. In each of these scenarios, the first laser pass was performed at 100 W. (a) The original voids are repaired (red) by the 100 W repair track, but new voids are created (blue) at the same depth. (b) The original voids are repaired (red) at 150 W, but new voids (blue) are created deeper in the substrate. (c) The repair track was run at 50 W and does not repair the existing voids (magenta). All laser passes have a scan speed of 144 mm s^{-1}.

This test of a void repair strategy using varying laser power demonstrates the difficulty in finding a laser power strong enough to access keyhole voids without producing new voids. However, this approach only investigates repair of keyhole porosity and it is entirely possible that such a remelting strategy could be an effective repair approach for voids formed by other mechanisms, such as lack of fusion or voids originating from the precursor powder. In any case, this study suggests that the melting of additional powder layers will not remove the voids formed at the base of the vapor depression in keyhole mode processing. If one considers building the next layer with the second scan with an additional 50-70 µm layer of powder on the surface, the vapor depression will not penetrate on average to the depth required to repair most of the voids created by the first pass. Thus, a void repair strategy using varying laser power with or without an additional powder layer added before the second laser scan, is not a workable approach.

3. X-ray diffraction of laser powder bed fusion

The underlying physics of powder melting, re-solidification, and subsequent recrystallization upon cooling during the laser powder bed fusion process is complex and remains poorly understood. The resultant thermal history and high thermal gradients upon and following resolidifcation from the melt determine the final phase fraction, microstructure (e.g. grain size and

orientation), and residual strain in a material, and thus the accompanying mechanical properties. We used high speed *in situ* X-ray diffraction to track phase and microstructure evolution in the titanium alloy Ti64 under LPBF-like conditions and to extract robust estimates of bulk cooling rates.

Figure 15 shows typical diffraction data collected from a 500 µm-thick Ti-64 substrate with a ~50 µm thick powder layer. These data were collected at a sampling rate of 500 Hz and 1 ms acquisition time per frame, with a 200 W laser scanned at 144 mm s^{-1}, and the X-ray beam center positioned ~50 µm below the powder substrate interface. This X-ray probe position simplifies analysis by precluding diffracted intensity contributions from flying spatter or powder particles. At the same time, since the melt depression and melt pool extend up to at least 100 µm below the powder substrate interface, the volume probed provides relevant information about the phase and microstructural evolution within a localized region undergoing melting and resolidification.

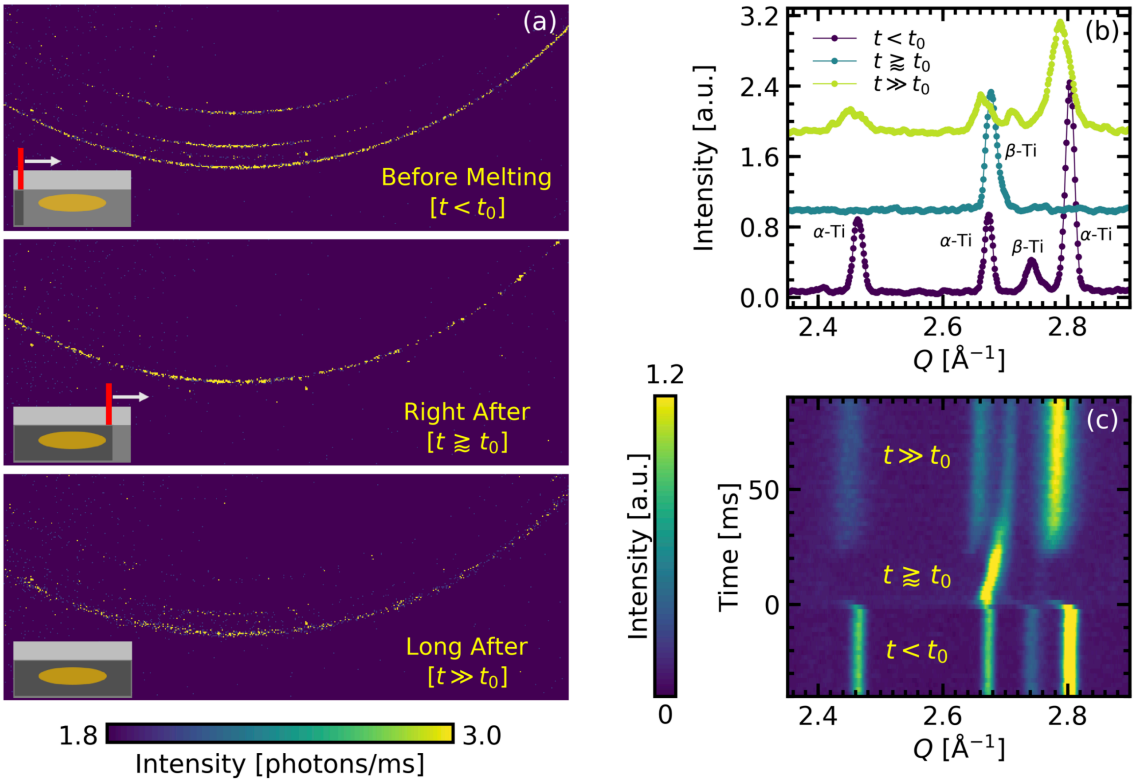

Figure 15. Diffraction data, collected at 500 Hz and 1 ms acquisition time per frame, for build parameters of 200 W laser power, 144 mm s^{-1} scan speed, and X-ray spot size 50 µm below the powder substrate interface. (a) 2D diffraction patterns ~10 ms before (top), t ~4 ms after (middle), and ~80 ms after (bottom) the laser scan. The insets show the positions of the laser relative to the X-ray probed region schematically at these times. (b) Corresponding azimuthally integrated intensities as a function of Q in blue, green and yellow respectively. (c) Integrated intensities plotted as a function of time on the vertical axis to show the evolution of the diffraction peaks during the LPBF process. The intensities for (a) and (c) are encoded by color with the scales indicated by the respective color bars.

Figure 15a shows 2D diffractograms ~10 ms before (top panel), ~4 ms after (middle panel), and ~80 ms after (bottom panel) the laser exposure. Azimuthally integrated intensities along Q of

these 2D diffraction patterns are plotted in Fig. 15b. Prior to laser melting, we see three clear α-Ti peaks ((100), (002), and (101)), and a small (110) β-Ti peak between the (002) and (101) α-Ti reflections, indicating that the unprocessed sample comprises a mix of α and β phases as expected with conventionally produced Ti64 at room temperature.[31–34] About 4 ms after the laser passes the probed volume (Fig. 15a middle panel, and Fig. 15b green circles), we see that most of the diffracted intensity is concentrated in one peak that we identify as the (110) β-Ti peak, implying that most of the probed volume at this point is above the β transus temperature. The position of the β-Ti peak right after the laser is significantly shifted towards smaller Q, which we attribute to thermal expansion of the crystal lattice. We also see a high Q tail to the β-Ti peak consistent with the variation in lattice parameters from the non-uniform temperature distribution within the probed volume that arises due to thermal gradients between the melted zone (MZ), the nearby unmelted but heat affected zone (HAZ), and the farther away unaffected zone. The kymograph in Fig. 15c shows the azimuthally integrated intensities encoded by color and stacked along the vertical time axis to follow the evolution of the diffracted peaks during the LPBF process. We see that for about 30 ms following laser melting, the diffraction intensity is mainly concentrated in the β-Ti peak. Over this time, the position of the β-Ti peak that had abruptly shifted to a smaller Q value immediately following laser melting, gradually shifts to higher Q as the lattice contracts upon cooling. After about 30 ms, a substantial fraction of the probed volume has cooled below the β transus, as evidenced by the abrupt reappearance of the α-Ti peaks that grow in intensity as that of the β-Ti peak diminishes. After ~100 ms, the peak positions and intensities remain nearly constant indicating the sample has reached thermomechanical equilibrium and the diffracted intensity is now redistributed between the low temperature α and β phases.

Comparing the final state to the initial state, we observe a number of changes to the material at ambient conditions. Even after a significant relaxation time allowing the material to return to room temperature, the diffraction peaks show a systematic shift towards lower Q, indicating a change in the bulk lattice constants that could arise from residual strain or a change in composition. The diffraction peaks are also noticeably broader, suggesting the possibility of smaller crystalline grains, enhanced microstrain, or a larger distribution of lattice parameters due to compositional or strain inhomogeneities. We note here that previous work has shown that LPBF of Ti-64 typically leads to a martensitic (α') phase due to the rapid cooling. [12,35–38] However, we cannot differentiate between the α and α' phases from the diffraction signals, and for brevity we will henceforth refer to this phase as α-Ti.

We next perform fitting analysis on the diffraction peaks to obtain a quantitative picture of the phase and microstructural evolution. Figure 16a plots the integrated intensities of the (101) α-Ti peak (purple circles) and the (110) β-Ti peak (green diamonds) as a function of time for laser power of 225 W and speed 144 mm s^{-1}. The moment the laser scans over the probed volume is shown by the vertical dashed line. Immediately following the laser, the intensity of the α-Ti peak drops to close to its minimum value over a span of ~4 ms as a fraction of the probed volume melts and resolidifies into the β-Ti phase, and then continues to drop more slowly over the next 10-15 ms as the thermal load is distributed over more of the probed sample volume heating it above the the β-transus temperature. The β-Ti peak intensity change follows the opposite trend as the α-Ti peak, though it lags the change in the α-Ti intensity by ~2 ms, which we note is the time resolution for this measurement. This lag in the response of the β-Ti peak can be understood as the initial melting and resolidification time following the laser. After that ~2 ms lag, the β-Ti peak jumps up to its near maximum value over a period of ~4 ms, like the decrease for the α-Ti peak, then

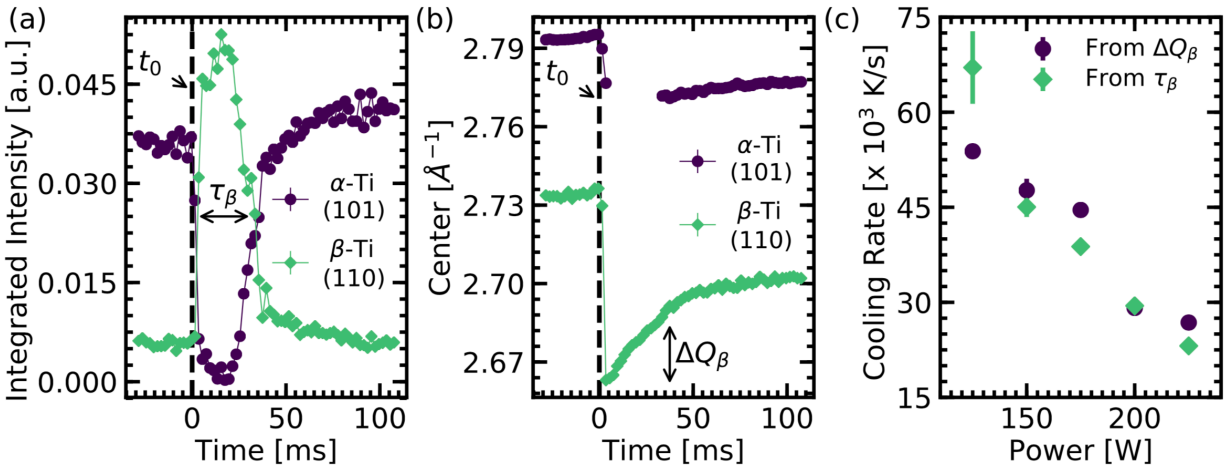

Figure 16. *In situ* cooling rates, calculated for data collected at 500 Hz and 1 ms acquisition time per frame. (a) Time evolution of integrated peak intensities of the α-Ti (purple circles) and β-Ti (green diamonds) reflections for laser power of 225 W and speed 144 mm s^{-1}. The drop in the alpha-Ti peak intensity coincides with the firing of the laser indicated by the dashed black line. Also, shown in the figure is the time period (τβ) for which the phase fraction is mainly β-Ti. The solid lines are guides for the eye. (b) Centers of the α -Ti (purple circles) and β-Ti peaks (green diamonds) as a function of time for same process parameters as (a). The change in the center of the β-Ti peak over τβ is indicated as ΔQβ. The centers of the α -Ti peak are not shown during τβ because of the large uncertainties in this time range. (c) Cooling rates for a range of laser powers calculated from rate of lattice relaxation (purple circles), and β-Ti lifetime, τβ (green diamonds). All other printing parameters other than the laser power are held fixed for these data points.

continues to increase more gradually over the next 10–15 ms. Also, the fact that we do not see a sharp drop in the total diffracted intensity at any measured time implies either that the melting and recrystallization happens at a time scale faster than we can resolve (< 2 ms) or that the melted volume is much smaller than the probed volume. We also note here that the speed of the laser scan (~144 mm s^{-1}) means that the duration for which the laser passes over the probed length (~300 μm) is about 2 ms, matching the detector frame rate. After the α-Ti and β-Ti peaks reach their minimum and maximum values respectively, they revert back to intensities closer to their starting values first rapidly over ~20 ms as the sample cools rapidly through the β-transus, and then more slowly as the low temperature α + β phase is stabilized.

Figure 16b plots the peak positions in reciprocal space of the (101) α-Ti peak (purple circles) and the (110) β-Ti peak (green diamonds) as a function of time for the same process parameters as Figure 16a. The inverse of the peak positions is proportional to the lattice constants, and hence this plot directly tracks the rate of change of the lattice parameters. The α-Ti peak position is roughly constant before laser melting (shown by the vertical dashed line), too broad to track reliably for about 30 ms after laser melting as the peak intensity drops sharply, and after that is found to have shifted by about 0.02 $Å^{-1}$ towards lower Q (~0.7% change) when the peak intensity has recovered sufficiently to determine the position again. This shift towards lower Q implies a larger lattice constant as compared to the initial state and can be attributed to a combination of thermal expansion, compositional variation, and/or tensile strain. Thereafter, it continues to shift more gradually towards higher Q values as thermal equilibrium is reached, but it does not recover

back to its original value. As there should be no residual thermal expansion at long times after the laser melting and resolidification, we can ascribe this shift in peak position to residual tensile strain in the direction probed by the X-rays (predominately in the plane normal to the incident X-rays), and/or a change in elemental composition. The β-Ti peak position (green diamonds), also roughly constant before the laser, moves abruptly to a lower Q value due to thermal expansion upon laser heating, and then shifts back to higher Q values as the sample cools down and the lattice contracts.

We now present two methods by which the above results are used to extract the *in situ* cooling rates after solidification. The first method involves determining the β-lifetime (τ_β) as shown in Fig. 16a, that we define as the time immediately following the laser induced melting and re-solidification for which the β-Ti phase is the predominant phase. As we see in Fig. 16a, the value of τ_β can be determined by following the time evolution of the intensities of the β-Ti peaks, or equivalently the α-Ti peaks. An asymmetric rectangular function with error functions to define the up and down steps is fit to the peak intensity, and τ_β is calculated as the distance between the centers of the two error functions. This corresponds to the time required for the probed sample volume to cool down from the melting point (~1870 K) to the β-transus temperature (~1270 K), below which the diffracted signal is again dominated by the primary α-Ti phase, and thus we obtain the average cooling rate over this temperature range. This method makes two simplifying assumptions. First, it does not consider undercooling that might lower the transition temperatures. However, since undercooling would lower both the melting and β-transus temperatures, the effect on the temperature differential between these two points, which is what is used for this calculation, is not expected to be large. As reported in another study,[23] undercooling lowers the melting temperature by ~40 K, and the error introduced by a change of this magnitude is accounted for by the error bars. Second, it does not explicitly consider the instantaneous thermal gradients within the probed volume. Here, we assume that even though the entire probed volume does not transition simultaneously across the β transus, the half maximum points of the error step functions used here to fit the intensity profiles during the transitions are a good approximation to the volumetric average.

The second method estimates the cooling rate from the rate of change of the β-Ti lattice constants as the sample cools through the β-Ti only phase. The positive shift in peak positions (ΔQ_β) during τ_β, as shown in Fig. 16b, is due to lattice contraction as the sample cools. If we attribute this contraction primarily to thermal contraction on cooling, we can use the known coefficient of thermal expansion for the relevant temperature range and fit the following expression obtained by applying Newtons law of cooling:

$$Q(t) = \frac{Q_0}{1 - CT_0(1 - e^{-Rt})} \qquad (2)$$

to the value of Q_β during τ_β to obtain an estimate of the rate, R. Here, Q(t) is the ΔQ_β at time t, Q_0 is the Q_β value at temperature T_0, C is the relevant coefficient of thermal expansion (~9 x 10^{-6} K^{-1}),[39] and R is the instantaneous rate at temperature T_0. By setting the melting temperature (~1870 K) as T_0, we get the cooling rate at the melting point and approximate it as the average cooling rate through the β-transus. This approach discounts contribution from residual strain and assumes that the dominant contribution to the instantaneous change in lattice parameter is from thermal expansion given the high cooling rate. The potential effect of compositional variations occurring within the probed volume during this period, τ_β, is also disregarded since diffusive transformations

are generally suppressed at such timescales,[12,35–38] and we assume no overall loss of material during this process.

Figure 16c shows the cooling rates, as a function of laser power with a constant laser scan speed of 144 mm s^{-1} and all other printing parameters held fixed, extracted using the two methods described above. The purple circles are cooling rates based on changes in β-Ti lattice constant, while the green diamonds show the values obtained from τ_β using the intensity time dependence of the (101) α-Ti peak. These cooling rates obtained by different methods are consistent within statistical uncertainties, which indicates these are robust estimates of the cooling rates despite the caveats listed above for each of the methods. This also suggests that the assumptions inherent to both approaches do not significantly affect the extracted cooling rate values, indicating that the undercooling of the melting transition and the β to α phase transition is comparable, and that no significant strain is developing over this cooling regime. As significant lattice shifts remain present in the final diffraction patterns, this also suggests that lattice strains only become significant after the material has cooled to below the β transus temperature. The highest cooling rate of ~6.5×10^4 K/s corresponds to the lowest laser power (125 W), and it decreases linearly to ~2.5×10^4 K/s as the power is ramped up to 225 W. The decreasing cooling rate implies smaller temperature gradients at higher powers between the melted and heat affected zones and the surrounding

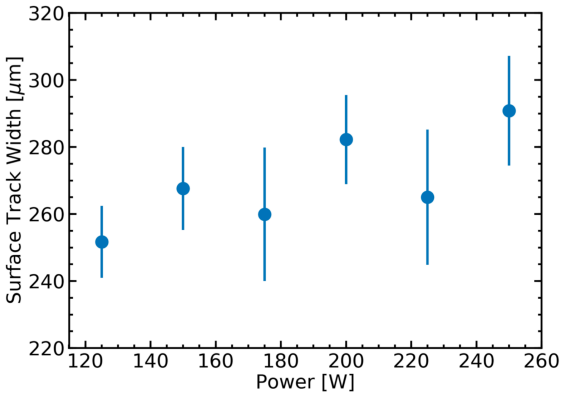

Figure 17. Surface track widths as a function of laser power for 144 mm s^{-1} scan speed measured *ex situ* using an optical microscope. These values and the error bars were obtained by taking the average and standard deviation of the track widths measured at three points close to the center of the track (the position of the X-ray probe.)

material that acts as the heat sink and includes regions outside the probed volume. This can be attributed to a higher temperature of the heat sink as the size of the melt pool grows with larger amounts of deposited energy. Figure 17 plots the surface track widths along the X-ray beam direction as a function of laser power. Since the width of the melt pool 50 μm below the interface scales with the surface track width,[40] we see that this width alone is not sufficient to account for the observed dependence of cooling rate on power. The depth of the melt pool also affects the thermal transport along the vertical direction and needs to be considered. Another factor to consider is the thermal dynamics in the melt involving Marangoni convection that would influence the thermal gradients after solidification and thus the post-solidification cooling rate. Finally, we cannot rule out the effect from non-ideal thermal boundary conditions at higher laser powers. Even though, as noted above, the thermal conductivities are comparable, the Ti-64 and glassy carbon

interface introduces additional thermal resistance that likely has an impact on the heat sink temperature.

To correlate the cooling rate with the final build, we now examine its effect on several characteristics of the final microstructure as summarized in Fig. 18. These plots show the relative changes between the initial pre-laser state and the final state measured ~1 s after laser exposure when we can assume thermal equilibrium. Figure 18a plots the change in the lattice spacing (d) of the α-Ti (102) and β-Ti (110) peaks, with purple circles and green diamonds respectively, as a function of cooling rate. We see that the change in the β-Ti phase has its highest value of ~1% at the lowest cooling rate and decreases monotonically with increasing cooling rate to a minimum value of ~0.3%. The α-Ti phase on the other hand shows a roughly constant 0.2% change with no dependence on the cooling rate. Thus, for all conditions considered here, we measure a lattice expansion in the direction perpendicular to the X-ray beam. As noted earlier, this expansion is attributed to residual tensile strain and/or compositional change. It is not straightforward to tease apart the relative contributions of these two effects from these data alone. Therefore, we performed energy dispersive spectroscopy (EDS) measurements on the cross-sectioned samples at Ames to examine the compositional variation in the different regions of the probed volume. Figures 19 and 20, and the associated tables (Tables 1 and 2), show that while the β phase in the HAZ and the region far from the HAZ is significantly V-rich (~12.5 wt.%), the MZ has a far more uniform V distribution (~3.6%) as the vanadium is redistributed over the entire melt volume and does not have time to partition to the β phase due to the high cooling rate. Since the lattice parameter of β phase increases with decreasing V content,[39,41] at least part of the β lattice change can be ascribed to this compositional change. However, if we again take the surface track widths as a measure of the melt pool width, we see from Fig. 17 that the change in the MZ fraction alone is insufficient to account for the lattice change, implying that the observed trend is due to increasing residual strain in the β phase with decreasing cooling rates. Since the prior β grains crystallize at a much higher temperature and cool far more rapidly before transforming into the α phase at a lower temperature, it is not unexpected that the remnant β phase bears most of the residual strain.

The change in peak widths, as shown in Fig. 18b, also shows a systematic dependence on cooling rate for the β-Ti phase (green diamonds), but not the α-Ti phase (purple circles). While the widths of both α-Ti and β-Ti peaks increase after re-solidification, the β-Ti peak widths also increase systematically with decreasing cooling rate. Diffraction peak widths, ignoring instrumental contributions, are affected by crystallite grain size, inhomogeneous microstrain, anisotropic macrostrain, and chemical inhomogeneity. We see immediately that the wider peaks are consistent with the corresponding higher values of residual strain at lower cooling rates. Another factor that contributes to the increased peak widths is the non-uniform distribution of lattice constants in the probed volume. The MZ, the HAZ and the unaffected zones have different microstructures as seen from back scattered electron (BES) imaging (Fig. 20). The measured peaks are a convolution of the diffraction from each of these regions. Since the peak shifts are larger for the smaller cooling rates, the measured peak widths would correspondingly be bigger at smaller cooling rates as well. One possibility to consider for increased peak widths is smaller crystallite size. But this does not fit with the observed trend of bigger widths at smaller cooling rates since slower cooling rates generally lead to larger crystallite size and therefore sharper diffraction peaks.[34] But this principle might not necessarily apply to grain sizes of intermediate metastable phases such as the β-Ti phase under consideration here, and so we cannot rule it out entirely.

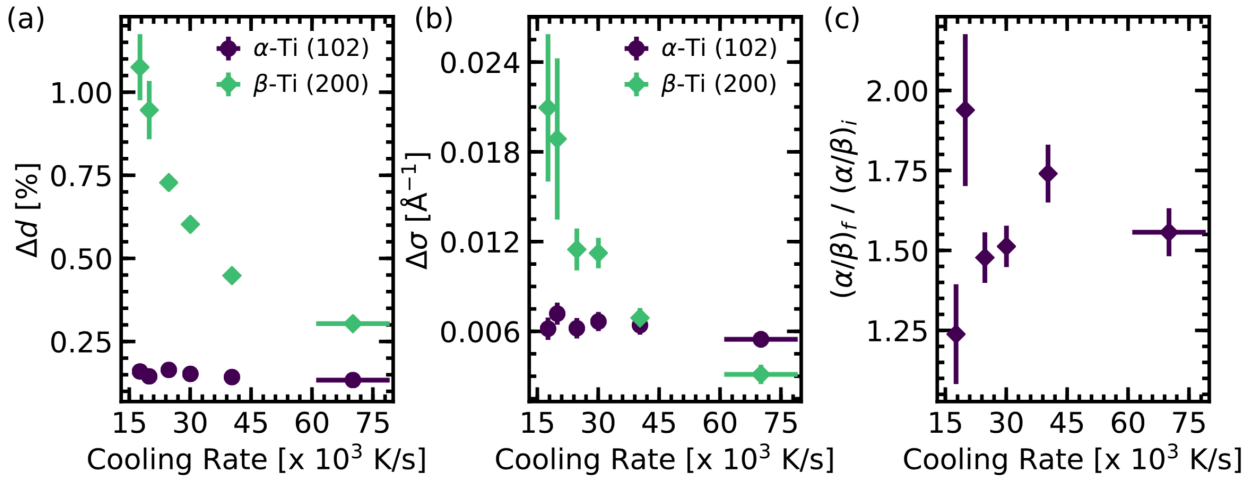

Figure 18. Correlating the cooling rates to changes in structural parameters and phase fraction of final build measured ~1 s after the laser exposure. These plots show the change in (a) lattice spacing, (b) peak widths, and (c) phase fraction (α-Ti / β-Ti) as a function of cooling rate calculated by taking the average cooling rates from the two methods outlined in the text and Fig. 16.

Finally, we look at the ratio of the relative fractions of the α-Ti and β-Ti phases before and after the fusion process, as plotted in Fig 18c. We see no systematic dependence of this ratio on the cooling rate, implying that while the microstructural properties of the α-Ti and β-Ti phases are intimately related to the cooling rate, the phase fraction itself remains unaffected. This observation

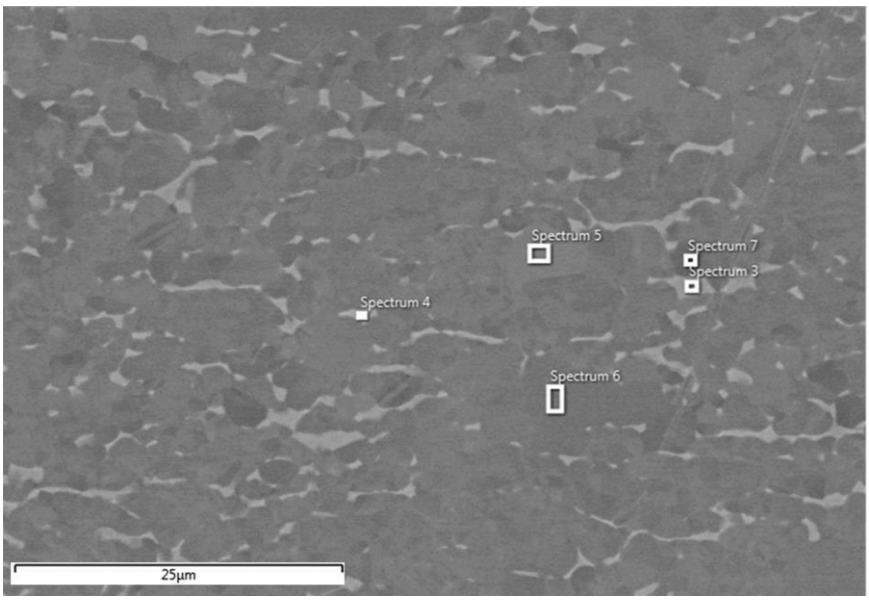

Figure 19. The backscattered electron (BSE) image of the base substrate far from the heat affected zone showing the vanadium rich β-Ti (bright regions) and darker gray vanadium poor α-Ti. The image was acquired using a FEI Teneo Field emission SEM operating at 15 kV.

disagrees with literature reports of the α to β ratio in LPBF parts, most of which report only α phase in as-built LPBF parts[42–44] while some report an α + β microstructure[45,46] indicating that the microstructure can indeed vary as a function of processing parameters. Our limited range of scan speed and power combinations may be confined to one of these two regimes. Furthermore, since this work focuses on single layer melting, we do not directly investigate if this variation in observed microstructure arises from initial solidification conditions, the subsequent cyclic rapid heating and cooling enforced by the LPBF process during a full build, or some interaction between these process parameters. We also cannot rule out texture effects in the small amount of β phase present in the final volume, which might raise uncertainty in the measurement.

Table 1. The energy dispersive spectroscopy (EDS) analysis of selected areas from Figure 19. Spectra 3 and 4 are from the vanadium rich β-Ti while spectra 5 - 7 are from the vanadium poor α-Ti regions. The Al was standardized using Al_2O_3 while the Ti and V were standardized using elemental standards. The data were acquired using an Oxford AztecHKL system on a FEI Teneo Field emission SEM operating at 15 kV using standard package for ZAF corrections. Values are in wt.% with uncertainty of ~5%.

	Spec 3	Spec 4	Spec 5	Spec 6	Spec 7
Al	3.10	3.53	5.95	6.07	6.00
Ti	82.64	83.95	91.50	91.61	91.49
V	14.26	12.52	2.55	2.32	2.51

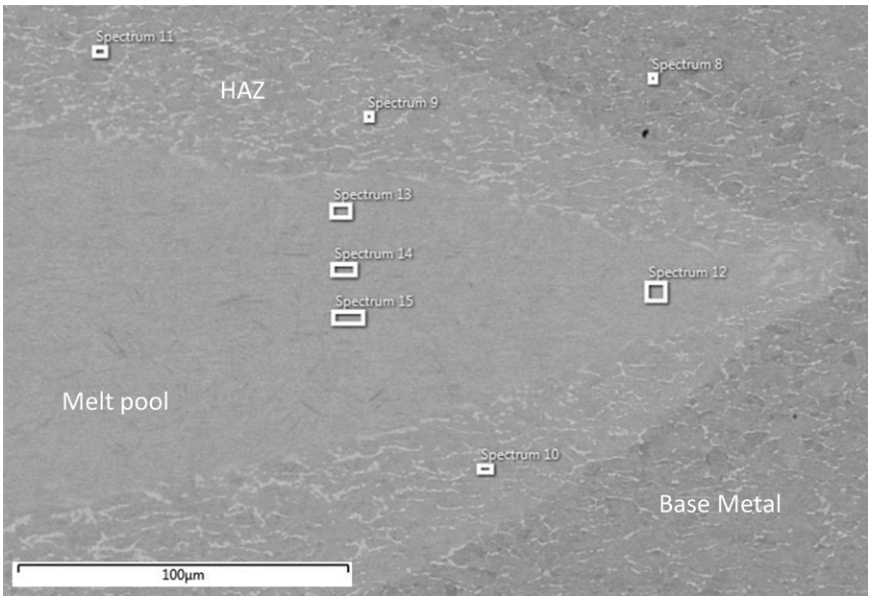

Figure 20. The BSE of the melt pool, heat affected zone (HAZ) and base substrate for a printed track with laser power of 225 W and 144 mm s^{-1} scan speed. The slight variation in the gray scale between the base metal and the HAZ is most likely due to subtle changes in the microstructure since the EDS did not show substantial changes in the α-Ti phase. The melt pool shows substantial changes in the microstructure and incorporation of more V into α-Ti (Table S2).

Table 2. EDS analysis of selected areas from Figure 20 showing that the composition of the α-Ti composition (gray phase) is virtually unchanged between the base metal (spectrum 8) and the HAZ (spectra 9 - 11). However, the melted zone (spectra 12 - 15) show substantial increase in the V. Data acquisition and analysis as described above. Further sampling of the composition of the melt pool from the surface to the bottom show virtually no change in the α-Ti.

	Spec 8	Spec 9	Spec 10	Spec 11	Spec 12	Spec 13	Spec 14	Spec 15
V	2.48	2.70	2.41	2.52	3.59	3.64	3.58	3.65
Al	5.97	5.95	5.98	5.98	5.74	5.74	5.75	5.73
Ti	91.55	91.61	91.61	91.51	90.66	90.62	90.76	90.63

3.1. Automated data analysis

In this section, we present an analysis of the AlCe and Ti64 *ex situ* diffraction data that involves developing methods to distinguish between potential microstructures (with distinctive crystallographic properties) that are formed in the melting process. We also discuss an analysis approach that can be used to extract information on boundaries, ideally size and shape, of different local microstructures found in the *ex situ* samples using the diffraction data. The *ex situ* diffraction data used in the analysis presented in this document is collected after the metal sample has re-solidified, post laser beam exposure. After the metal sample has re-solidified and cooled, we expect it to retain microstructures generated due to laser exposure such as melt pool, heat affected zone and un-melted regions.

In order to study characteristics of these different microstructures, diffraction data was collected for various cross-sectional segments of the re-solidified sample. *In situ* test samples were cut in order to expose the cross section of the laser melted area. These cross sections were then scanned using a 30 µm x 60 µm x-ray beam which was rastered across the entire sample area. Each of the squares in Figure 21 represents a region in the cross-sectional sample for which diffraction data is collected. In the analysis presented in this document, we use the integrated intensity distributions obtained from integrating the intensities, from the diffraction patterns, along Q.

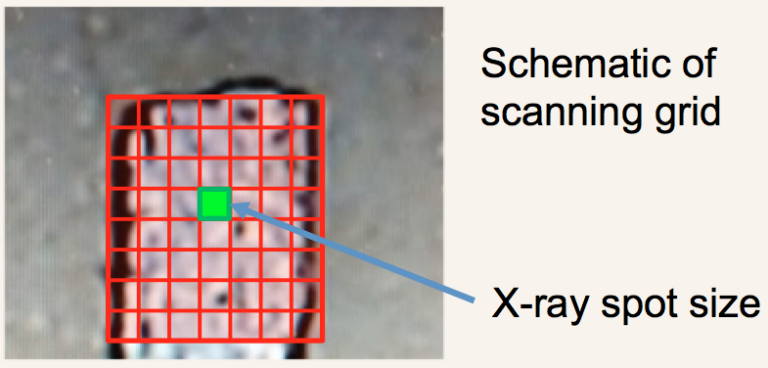

Figure 21. Schematic view of diffraction data collection process across the sample.

In this analysis, we used the integrated intensity distributions obtained from diffraction data corresponding to different regions scanned in the cross-sectional slice of the cooled, re-solidified sample to answer two main questions (a) are there are crystallographically different regions (microstructures) in the sample and (b) how do these regions differ (in terms of peak

location, width in the integrated intensity distributions), giving us information about the underlying crystalline structure.

In order to extract similarity level of different scanned regions in a given sample, we constructed some features (variables) that are used to assess vector/image/distribution similarity. Three main variables are used to assess similarity level between integrated intensity distributions I(Q) from different regions of the cross-sectional sample. These variables are constructed using the integrated intensity distributions are Cosine similarity, L2-Norm, and the Kolmogorov-Smirnov test. We describe them below in detail.

The Cosine similarity is a heavily used concept in data analysis used to assess directional similarity level between two vectors. Consider two vectors in two-dimensional space (X1, X2). Cosine distance is defined as the angle θ between these vectors. Cosine similarity is defined as cos(θ). If two given vectors are close to each other in space, then the angle between them will be small and cos(θ) will be close to 1. For very differently spaced vectors, cos(θ) will be closer to 0 since the angle between the vectors will be higher. By design, cosine similarity value will always be between 0 (no similarity) and 1 (completely similar).

For the *ex situ* data analysis, we consider I(Q) from two different regions as vectors (I_1 and I_2) and calculate the cosine similarity between them, as follows:

$$\cos(\theta; I_1, I_2) = \frac{I_1 \cdot I_2}{|I_1||I_2|} \qquad (3)$$

The above calculation is the same as calculating the scalar or dot product between two vectors and dividing by the magnitudes of the two vectors.

For *ex situ* diffraction data, if the two vectors of I(Q)s are different, then cosine similarity between them will be closer to 0. If cosine similarity is 1, then the two vectors of I(Q)s are exactly the same (since angle between the two vectors would be zero). The cosine similarity feature gives us a measure of similarity between peak positions of two integrated intensity distributions. However, if two I(Q)s have the same peak positions but different magnitudes, then cosine similarity will not capture the difference in peak magnitudes since this feature only gives information about directional differences.

The L2-Norm is used heavily in machine learning, especially for regularizing and normalizing data. It can also be used to assess similarity level between two given distributions. L2-Norm between two integrated intensity distributions (vectors) I_1 and I_2 is defined as $\sqrt{\sum_i^N (I_{1i} - I_{2i})^2}$, where I_1 and I_2 are two independent integrated intensity distributions to be compared and N is the total number of points in these distributions. If at a given value of *i* the two distributions have very different magnitudes, then the corresponding term in L2-Norm calculation will be larger. If the two distributions are exactly the same, then at each value of *i* their magnitude will be the same, resulting in L2-Norm equal to 0. The more diverse two given distributions are, the higher the value of L2-Norm will be.

The third set of variables that is used to assess similarity between two integrated intensity distributions is obtained using the Kolmogorov-Smirnov (KS) test. The KS test is a nonparametric test widely used in statistics to assess the equality of two continuous, one-dimensional distributions such as (a) a sample/distribution with a reference probability distribution (one-sample K–S test) or (b) to compare two samples/distributions (two-sample K–S test).

The Kolmogorov–Smirnov statistic quantifies a distance between the empirical distribution function of the sample and the cumulative distribution function of the reference distribution, or

between the empirical distribution functions of two samples. The null distribution of this statistic is calculated under the null hypothesis that the sample is drawn from the reference distribution (in the one-sample case) or that the samples are drawn from the same distribution (in the two-sample case). In each case, the distributions considered under the null hypothesis are continuous distributions but are otherwise unrestricted.

The two-sample KS test is one of the most useful and general nonparametric methods for comparing two samples, as it is sensitive to differences in both location and shape of the empirical cumulative distribution functions of the two samples. The KS statistic (or distance) is 0 if the distributions are exactly the same, with a p-value of 1 (i.e. 100% confidence in the hypothesis that the two distributions are drawn from the same parent distribution). If the distributions are different then the KS statistic has a value higher than zero with a different p-value (ranging between 0 and 1, giving a degree of confidence in rejecting the null hypothesis that the two distributions are drawn from the same parent distribution).

We use all the variables described above to find microstructures in the cross-sectional *ex situ* samples that have similar crystallographic properties. In order to find similar regions (clusters) or microstructures, we use clustering methods that are commonly used in machine learning. Cluster analysis or clustering is the task of grouping data in such a way that data points in the same group (called a cluster) are more similar (in some sense) to each other than to those in other groups (clusters). It is a main task of exploratory data mining, and a common technique for statistical data analysis.

We found that hierarchical clustering, which builds clusters incrementally and the total number of clusters does not need to be specified prior to the clustering, provided robust results with regions that matched well with SEM performed by Ames. An example of a resulting cluster map for one of the Ti64 cross-sections is given in Figure 22. The color indicates individual clusters. In this case, five clusters were used. Clusters 1 (green) and 2 (blue) are likely background and clusters 3 (brown), 4 (other brown), and 5 (teal) are likely regions within the cross-section with distinct microstructure that map to different cooling rates and heating histories.

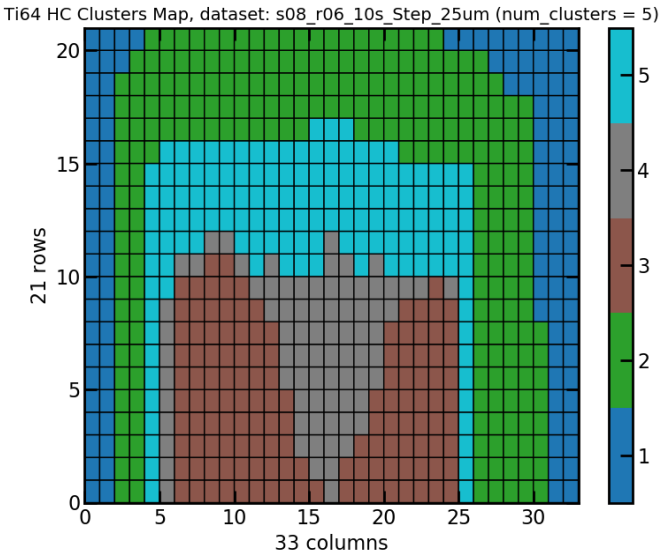

Figure 22. Example of a cluster map for one of the Ti64 cross-sections. The color indicated the different regions with very similar diffraction patterns.

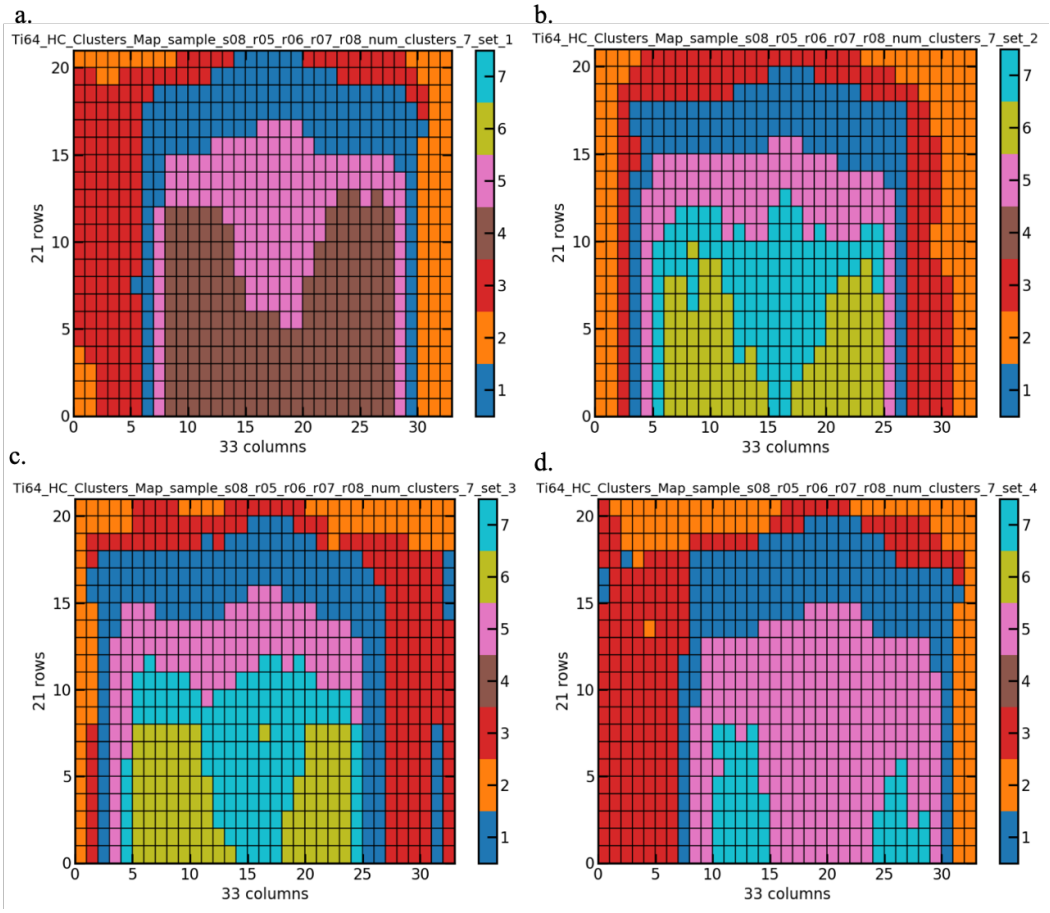

Figure 23. Combined cluster analysis on four different cross-sections with four different laser powers. The lowest power is panel (a) and the highest is panel (d). Although most of the regions are shared between samples, only (a) has region 4 (brown). Moreover, (d) does not have region 6 (yellow).

We also ran clustering analysis on a combined Ti64 dataset with four different laser powers in order to examine if there are any crystallographically similar regions across different samples. This would tell us, for example, if the microstructure of the heat pool was independent of the laser scanning parameters. With seven total clusters we found most, but not all, of the cross-sections had similar microstructure regions (Figure 23). The cross-section with the lowest laser power is Figure 23a. It is the only cross-section with region 4 (brown). This may mean that the laser power was low enough to not create microstructures that are present in the other three samples. The cross-section in Figure 23d on the other hand was exposed to the highest laser power amongst the four samples. We see that the cluster 6 (yellow) is present in Figure 23b and d, but not seen in Figure 23d. One reason of not observing the yellow cluster in the cross-section with the highest laser power could be that the sample needed to be scanned more deeply (further down) in order to scan a region that may be part of this region. Or it is possible that cluster 6 was not formed in this sample in the range of laser power sample was exposed to. These results are being compared to the SEM data collected by Ames which show explicitly the depth and width of the melt pool and the extent of the HAZ (Figure 24).

Analysis of *ex situ* diffraction data, specifically integrated intensity distributions I(Q), shows that 1-dimensional I(Q) distributions have reasonable information to distinguish between local microstructures that are formed when Ti64 samples are exposed to lasers. Clustering analysis of these I(Q) distributions provides useful information on the shape and size of some microstructures that have similar crystallographic properties. Clustering analysis on samples that have been exposed to different laser power also gives some interesting insights into how these microstructures may be created or change (in size or shape) with increasing laser power. As the next step, it would be useful to analyze the physical properties of these microstructures (clusters) and examine if their crystallographic properties can be mapped to different physical zones created in the melting process, such as melt pool, heat-affected zone or un-melted zones.

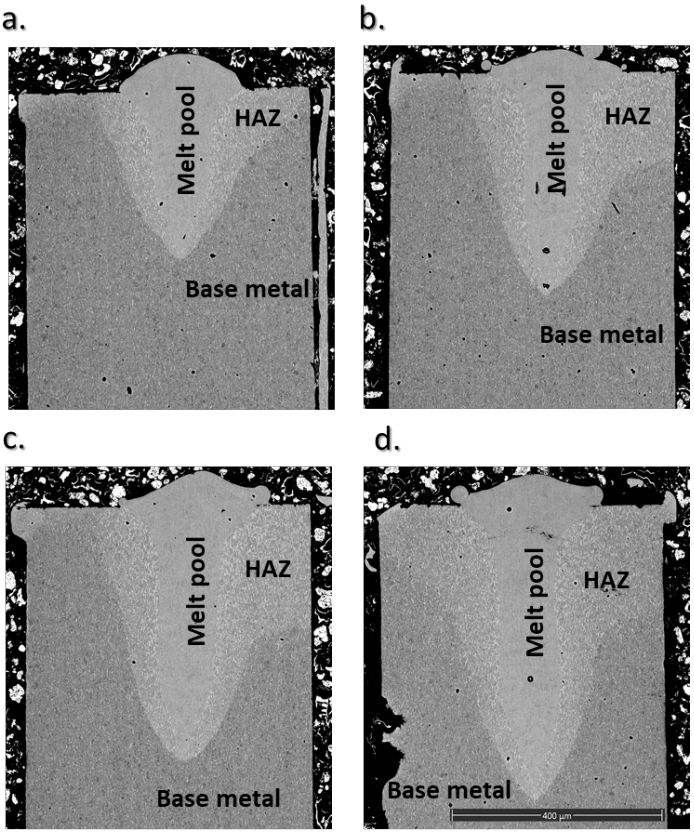

Figure 24. Backscattered scanning electron images for the same four cross-sections in Figure 23. Note that the depth of the melt pool and the extent of the HAZ both systematically increase with increasing laser power.

4. Flexible powder feed system for *in situ* X-ray characterization

The team at Ames Laboratory with consultation from SLAC designed a custom flexible powder feed system for *in situ* X-ray characterization of directed energy deposition. This system has multi-axes of motion including tilt (Figure 25a), while the print head (Fig. 25b) has two additional axes of motion. The detector holder (Fig. 25c) allows the detector to move forward and backward relative to the melt pool/build, which is housed inside the glovebox chamber (Fig. 25d).

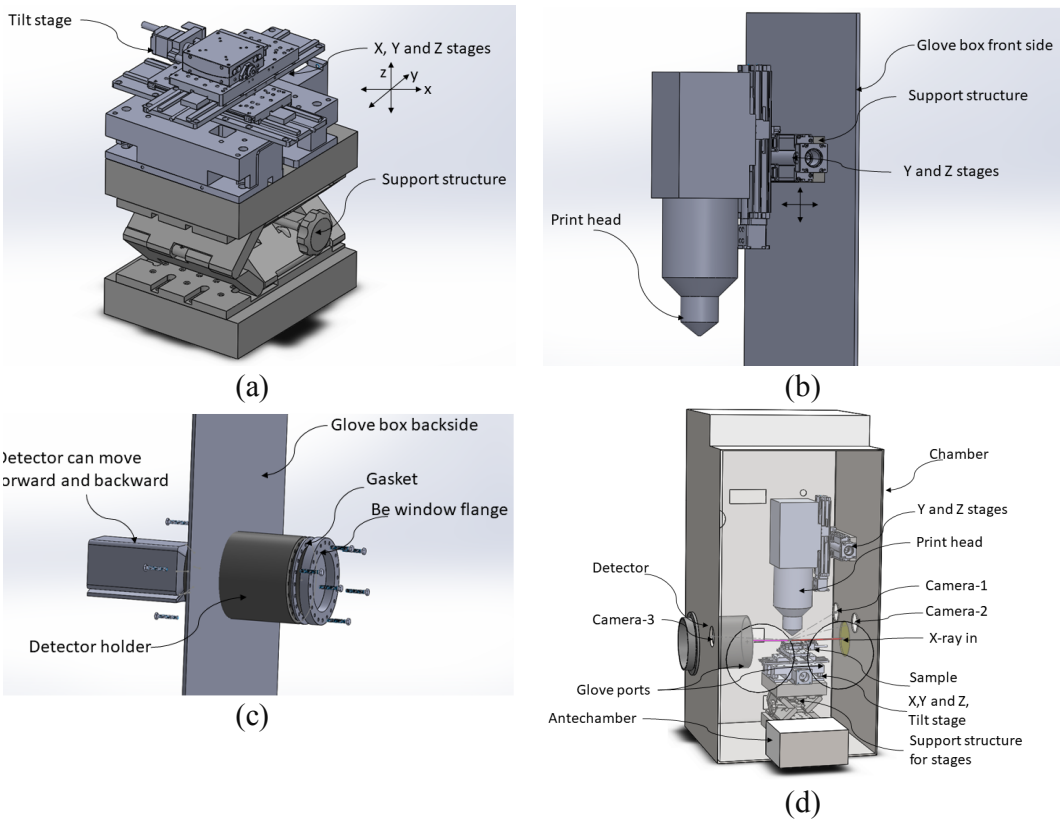

Figure 25. CAD models of (a) flexible base stage, (b) print head mount, (c) detector holder, and (d) flexible multi-layer powder feed system.

5. Powder characterization at Ames

With the increasing adoption of AM technologies, powder synthesis has become increasingly more important. For the Ti64 alloy composition, several commercial vendors produce powders by different technologies including gas atomization, plasma atomization, plasma rotating electrode process (PREP) and electrode induction gas atomization (EIGA). The team at Ames characterized the chemistry, morphology (e.g. porosity) and flow behavior of Ti64 powders from several vendors synthesized by various different methods.

Scanning Auger was performed to characterize the thickness of the oxide layer on the different powders. While the range of measured oxide thicknesses ranged from 5-12 nm for the different powder sizes, no obvious correlation with powder size could be found.

The oxygen, nitrogen, carbon, and sulfur content in the powders was measured by Laboratory Equipment Corporation (LECO) analysis (Figure 26). Interestingly, the smaller powders did not show higher oxygen content relative to the large powders. Furthermore, the Grade 23 AP&C (+10/-45 mm) exhibited higher oxygen than its Grade 5 counterpart, which is opposite of what is expected.

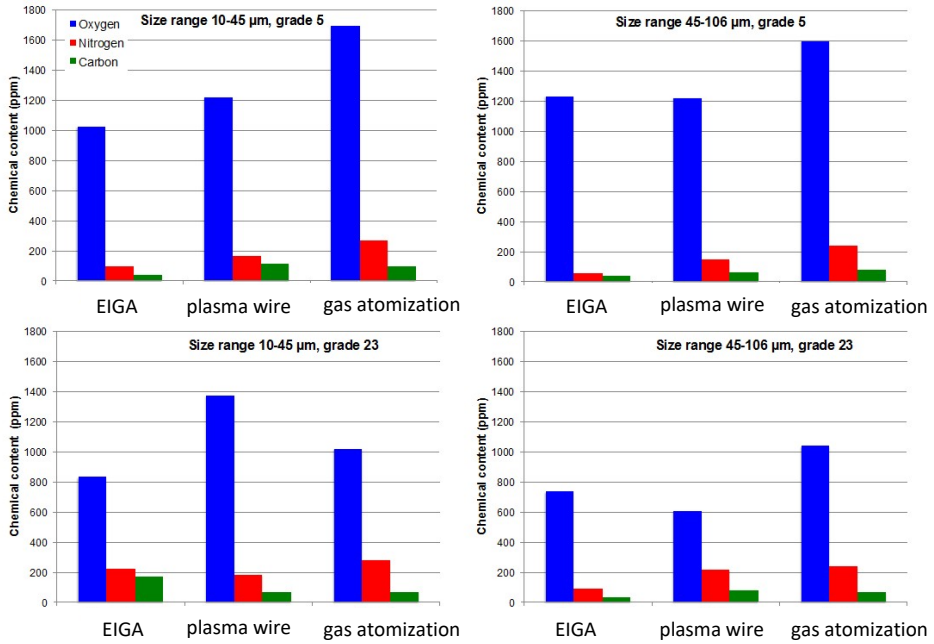

Figure 25. Oxygen, nitrogen, carbon, and sulfur content in powders produced using EIGA, plasma wire atomization, and gas atomization measured by LECO analysis. In general, the larger grades have smaller oxygen content.

Microtrac measurements were done on the powder for comparison with the particle size ranges specified by the vendors. Additionally, the flow rates of the different powders have been characterized using the Hall Flow method (Figure 26). A summary of the flow rates (lower number represents better flow) for the +45/-106 µm powders are shown below. It should be noted that that powder beds typically use powder sizes < 45 µm; however, small powders sizes are well-suited standard Carney or Hall flow measurements, and thus, not the focus of this work.

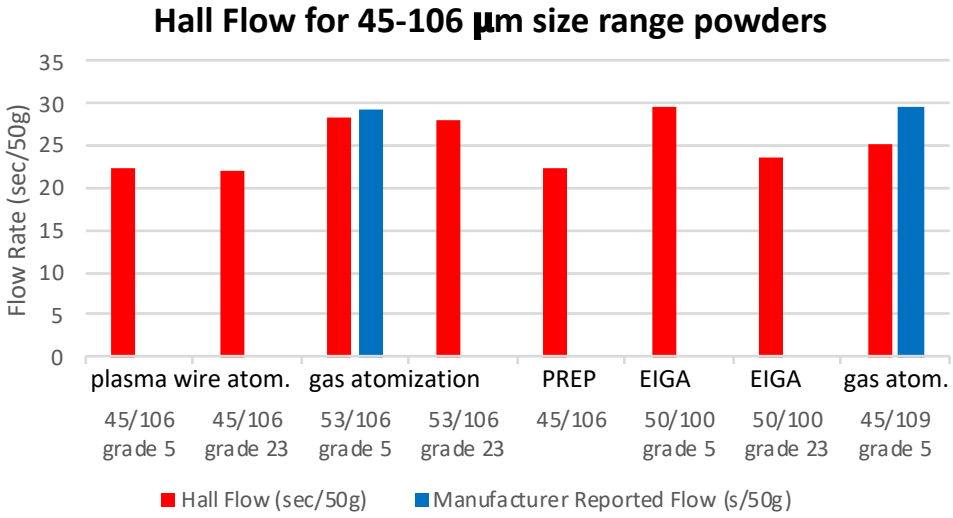

Figure 26. Flow rates of different powders produced using plasma wire atomization, gas atomization, PREP, and EIGA measured by ASTM standard Hall Method. A lower flow rate corresponds to better flow.

Finally, SEM images have been taken of the bulk powders to characterize the surface morphology (Figure 27). The plasma wire atomization and PREP powders have smooth particles with very little surface porosity or satellite particles. Whereas the EIGA and gas atomization powders all have rough surfaces with noticeable porosity, satellite particles, and oblong or deformed particles.

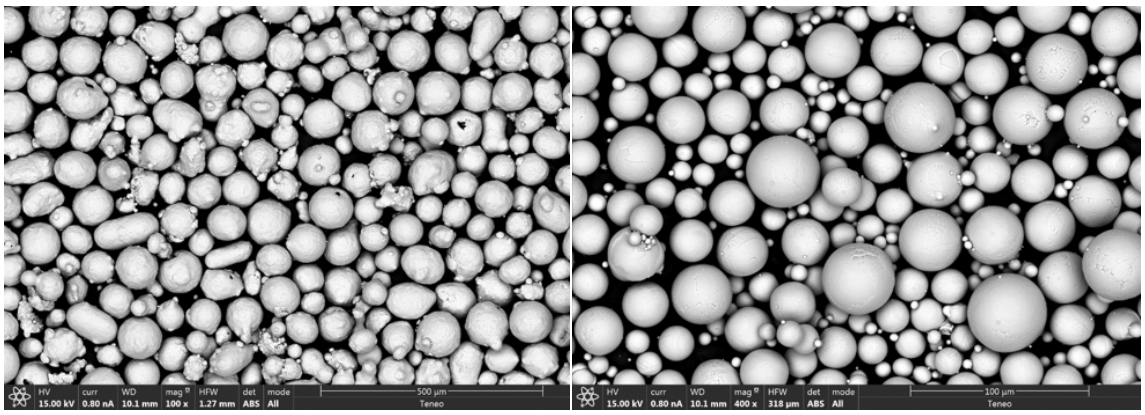

Figure 27. SEM images of the gas atomoization 53/106 grade 5 powder (left) and plasma wire atomization 10/45 grade 23 powder (right).

Benefits Assessment

The *in situ* X-ray characterization tools developed from this project enable the rapid validation of models and the more rapidly qualify parts. Additionally, they allow us to easily measure for the first time physical parameters such as the cooling rate of the solid as valuable inputs to these same models. With more reliable model inputs and methods to rapidly validate these models, AM machine makers and users can now have a better understanding of the connection between process parameters and the properties of the final build. This gives them control over builds down to the microscopic level. This control opens up additive manufacturing to a wider community reducing the need for traditional machining processes and enable machining of parts designed for energy efficiency, such as more compact and efficient cooling systems. Additive manufacturing can save on the transportation and storage of spare parts by enabling parts to be made as needed on location.

Finally, with this control over the process, we can begin to explore novel materials inaccessible to traditional machine methods. The properties of these materials can be tailored to the requirements of the part and its specific use. For example, we can tune local strain in a part to control distortion or increase strength in a particular direction. We can also begin to understand the added complexity when dissimilar materials such as metals and ceramics are printed together or tune the physical properties of an interface with microscopic precision. With the gained understanding of the AM processes from our *in situ* X-ray characterization toolset, the AM community will be able to realize the full potential of the technology.

Commercialization

The importance of *in situ* X-ray characterization of laser powder bed fusion has been acknowledged by the additive manufacturing community with interest in utilizing the tool and/or

the data and knowledge generated by it. We currently have single layer printing capability with both *in situ* X-ray imaging and diffraction characterization available. These have been tested on a number of different Ti, Al, and Mg alloys. In addition to the turnaround study highlighted above, we can also study similarly common printing strategies such as the complications that arise with printing an overhang where print layers tend to sag because of the transition from printing on solid metal to lose powder.

In addition to the current capabilities, we are seeking out opportunities to expand our capabilities to include multilayer printing using laser powder bed fusion and implementing a flexible multilayer system using directed energy deposition (see Section 4 of the Results and Discussion for the design concept). We anticipate these two additional capabilities will dramatically increase the types of processing conditions we can explore and deepen the understanding of the AM processes, which will in turn increase the commercialization potential.

Finally, because of the requirement of very bright synchrotron radiation for these *in situ* characterization techniques, correlating the thermal and optical surface probes which we have tested on our system with the subsurface information from X-rays will enable understanding of the LPBF process to move beyond simple scans to full builds. Once the data from inline surface diagnostic tools are correlated with the *in situ* X-rays, it will allow the industry to detect undesired properties such as voids while a part is being built on the production line. Once detected the machine can make the decision to start the print over again with modified parameters to avoid repeating the defect or initiate a repair strategy to fix the part before it is completed.

Accomplishments

Publications:

1. Calta, N. P.; Wang, J.; Kiss, A. M.; Martin, A. A.; Depond, P. J.; Guss, G. M.; Thampy, V.; Fong, A. Y.; Nelson Weker, J.; Stone, K. H.; Tassone, C. J.; Kramer, M. J.; Toney, M. F.; Van Buuren, A.; Matthews, M. J. An instrument for *in situ* time resolved X-ray imaging and diffraction of laser powder bed fusion additive manufacturing processes. *Review of Scientific Instruments*, **2018**, *89*, 055101. [Editor's Choice]
2. Martin, A. A.; Calta, N. P.; Khairallah, S. A.; Wang, J.; Depond, P. J.; Fong, A. Y.; Thampy, Y.; Guss, G. M.; Kiss, A. M.; Stone, K. H.; Tassone, C. J.; Nelson Weker, J.; Toney, M. F.; Van Buuren, A.; Matthews, M. J. Dynamics of pore formation during laser powder bed fusion additive manufacturing. *Nature Communications. Accepted*.
3. Kiss, A.; Fong, A.; Calta, N.; Thampy, V.; Martin, A.; Depond, P.; Wang, J.; Matthews, M.; Ott, O.; Tassone, C.; Stone, K.; Kramer, M.; van Buuren, A.; Toney, M.; Nelson Weker, J. Void Defect Dynamics Near the Keyhole Threshold during Laser Powder Bed Fusion Additive Manufacturing. *Submitted for publications*.
4. Thampy, V., Fong, A. Y; Calta, N. P; Wang, J.; Martin, A. A.; Depond, P. J.; Kiss, A. M.; Guss, G. M, Xing; Q; Ott, R. T; Van Buuren, A.; Toney, M. F.; Weker, J. N.; Kramer, M. J.; Matthews, M. J.; Tassone, C. J.; Stone, K. H., Cooling Rates and

Structural Response during Laser Based Metal Additive Manufacturing. *Submitted for publications*.

Theses:

Work from this project is part of a Master's thesis by Alden Watts.

Software:

The cluster analysis code for analyzing *ex situ* XRD maps is published on SLAC's GitHub https://github.com/slaclab/AM_ExSitu_Clustering_Analysis

Conclusions

We have successfully designed and demonstrated a laser powder bed fusion testbed that enables subsurface X-ray monitoring with both diffraction (at 3 kHz) and imaging (at 20 kHz). Additionally, this testbed incorporates standard optical-based, melt pool monitoring similar to what is available on most full scale LPBF machines. Thus, we can link X-ray characterization available only at a synchrotron with standard optical tools and advanced modeling available at for example LLNL. The importance of these tools has been acknowledged by the additive manufacturing community with interest in utilizing the tool and/or the data and knowledge generated by it from General Motors, Aerojet Rocketdyne, United Technologies Research Center, General Electric, FormAlloy, NUBURU, Nano Al, Arconic, BeAM Machines, Bosch, Renishaw, and ESI.

References

1. Matthews, M. J. *et al.* Denudation of metal powder layers in laser powder bed fusion processes. *Acta Mater.* **114**, 33–42 (2016).
2. Ly, S., Rubenchik, A. M., Khairallah, S. A., Guss, G. & Matthews, M. J. Metal vapor micro-jet controls material redistribution in laser powder bed fusion additive manufacturing. *Sci. Rep.* **7**, 4085 (2017).
3. Trapp, J., Rubenchik, A. M., Guss, G. & Matthews, M. J. In situ absorptivity measurements of metallic powders during laser powder-bed fusion additive manufacturing. *Appl. Mater. Today* **9**, 341–349 (2017).
4. Bidare, P., Maier, R. R. J., Beck, R. J., Shephard, J. D. & Moore, A. J. An open-architecture metal powder bed fusion system for in-situ process measurements. *Addit. Manuf.* **16**, 177–185 (2017).
5. Bidare, P., Bitharas, I., Ward, R. M., Attallah, M. M. & Moore, A. J. Fluid and particle dynamics in laser powder bed fusion. *Acta Mater.* **142**, 107–120 (2018).
6. Pavlov, M., Doubenskaia, M. & Smurov, I. Pyrometric analysis of thermal processes in SLM technology. *Phys. Procedia* **5**, 523–531 (2010).
7. Lane, B., Moylan, S., Whitenton, E. P. & Ma, L. Thermographic measurements of the commercial laser powder bed fusion process at NIST. *Rapid Prototyp. J.* **22**, 778–787 (2016).
8. Fox, J. C., Lane, B. M. & Yeung, H. Measurement of process dynamics through coaxially

aligned high speed near-infrared imaging in laser powder bed fusion additive manufacturing. in (eds. Bison, P. & Burleigh, D.) **10214**, 1021407 (International Society for Optics and Photonics, 2017).
9. Furumoto, T., Ueda, T., Alkahari, M. R. & Hosokawa, A. Investigation of laser consolidation process for metal powder by two-color pyrometer and high-speed video camera. *CIRP Ann.* **62**, 223–226 (2013).
10. Rodriguez, E. *et al.* Approximation of absolute surface temperature measurements of powder bed fusion additive manufacturing technology using in situ infrared thermography. *Addit. Manuf.* **5**, 31–39 (2015).
11. Kanko, J. A., Sibley, A. P. & Fraser, J. M. In situ morphology-based defect detection of selective laser melting through inline coherent imaging. *J. Mater. Process. Technol.* **231**, 488–500 (2016).
12. Elmer, J. W., Palmer, T. A., Babu, S. S., Zhang, W. & DebRoy, T. Phase transformation dynamics during welding of Ti-6Al-4V. *J. Appl. Phys.* **95**, 8327–8339 (2004).
13. Elmer, J. W., Palmer, T. A. & Wong, J. *In situ* observations of phase transitions in Ti–6Al–4V alloy welds using spatially resolved x-ray diffraction. *J. Appl. Phys.* **93**, 1941–1947 (2003).
14. Elmer, J. W., Wong, J. & Ressler, T. Spatially resolved X-ray diffraction phase mapping and $\alpha \rightarrow \beta \rightarrow \alpha$ transformation kinetics in the heat-affected zone of commercially pure titanium arc welds. *Metall. Mater. Trans. A* **29**, 2761–2773 (1998).
15. Babu, S. S., Elmer, J. W., Vitek, J. M. & David, S. A. Time-resolved X-ray diffraction investigation of primary weld solidification in Fe-C-Al-Mn steel welds. *Acta Mater.* **50**, 4763–4781 (2002).
16. Palmer, T. A., Elmer, J. W. & Wong, J. observations of ferrite – austenite transformations in duplex stainless steel weldments using synchrotron radiation. *Sci. Technol. Weld. Join.* **7**, 159–171 (2002).
17. Wong, J., Ressler, T. & Elmer, J. W. Dynamics of phase transformations and microstructure evolution in carbon–manganese steel arc welds using time-resolved synchrotron X-ray diffraction. *J. Synchrotron Radiat.* **10**, 154–167 (2003).
18. Yonemura, M. *et al.* <I>In-Situ</I> Observation for Weld Solidification in Stainless Steels Using Time-Resolved X-ray Diffraction. *Mater. Trans.* **47**, 310–316 (2006).
19. Khairallah, S. A., Anderson, A. T., Rubenchik, A. & King, W. E. Laser powder-bed fusion additive manufacturing: Physics of complex melt flow and formation mechanisms of pores, spatter, and denudation zones. *Acta Mater.* **108**, 36–45 (2016).
20. Zhao, C. *et al.* Real-time monitoring of laser powder bed fusion process using high-speed X-ray imaging and diffraction. *Sci. Rep.* **7**, 3602 (2017).
21. Parab, N. D. *et al.* Ultrafast X-ray imaging of laser–metal additive manufacturing processes. *J. Synchrotron Radiat.* **25**, 1467–1477 (2018).
22. Cunningham, R. *et al.* Keyhole threshold and morphology in laser melting revealed by ultrahigh-speed x-ray imaging. *Science (80-.).* **363**, 849 LP-852 (2019).
23. Kenel, C. *et al.* In situ investigation of phase transformations in Ti-6Al-4V under additive manufacturing conditions combining laser melting and high-speed micro-X-ray diffraction. *Sci. Rep.* **7**, 16358 (2017).
24. Calta, N. P. *et al.* An instrument for in situ time-resolved X-ray imaging and diffraction of laser powder bed fusion additive manufacturing processes. *Rev. Sci. Instrum.* **89**, 55101 (2018).

25. Hann, D. B., Iammi, J. & Folkes, J. A simple methodology for predicting laser-weld properties from material and laser parameters. *J. Phys. D. Appl. Phys.* **44**, 445401 (2011).
26. King, W. E. *et al.* Observation of keyhole-mode laser melting in laser powder-bed fusion additive manufacturing. *J. Mater. Process. Technol.* **214**, 2915–2925 (2014).
27. Mills, K. C. Ti: Ti-6 Al-4 V (IMI 318). in *Woodhead Publishing Series in Metals and Surface Engineering* (ed. Mills, K. C. B. T.-R. V. of T. P. for S. C. A.) 211–217 (Woodhead Publishing, 2002). doi:https://doi.org/10.1533/9781845690144.211
28. Groeber, M. A. *et al.* Application of characterization, modelling, and analytics towards understanding process-structure linkages in metallic 3D printing. *IOP Conf. Ser. Mater. Sci. Eng.* **219**, 12002 (2017).
29. Martin, A. A. *et al.* Dynamics of pore formation during laser powder bed fusion additive manufacturing. *Nat. Commun.*
30. Yasa, E., Deckers, J. & Kruth, J. The investigation of the influence of laser re-melting on density, surface quality and microstructure of selective laser melting parts. *Rapid Prototyp. J.* **17**, 312–327 (2011).
31. Kobryn, P. A. & Semiatin, S. L. Microstructure and texture evolution during solidification processing of Ti-6A1-4V. *J. Mater. Process. Technol.* **135**, 330–339 (2003).
32. Gockel, J. & Beuth, J. Understanding Ti-6Al-4V Microstructure Control in Additive Manufacturing via Process Maps. *Solid Free. Fabr. Proc.* 666–674 (2013). doi:10.1007/s11837-005-0029-x
33. Kobryn, P. A. & Semiatin, S. L. The laser additive manufacture of Ti-6Al-4V. *JOM* **53**, 40–42 (2001).
34. Lutjering, G. & J C Williams. *Titanium, Second Edition*. (Springer International Publishing, 2007).
35. Murr, L. E. *et al.* Microstructure and mechanical behavior of Ti-6Al-4V produced by rapid-layer manufacturing, for biomedical applications. *Journal of the Mechanical Behavior of Biomedical Materials* **2**, 20–32 (2009).
36. Ahmed, T. & Rack, H. J. Phase transformations during cooling in α+β titanium alloys. *Mater. Sci. Eng. A* **243**, 206–211 (1998).
37. Simonelli, M., Tse, Y. Y. & Tuck, C. The formation of α + β microstructure in as-fabricated selective laser melting of Ti–6Al–4V. *J. Mater. Res.* **29**, 2028–2035 (2014).
38. Yang, J. *et al.* Formation and control of martensite in Ti-6Al-4V alloy produced by selective laser melting. *Mater. Des.* **108**, 308–318 (2016).
39. Elmer, J. W., Palmer, T. A., Babu, S. S. & Specht, E. D. In situ observations of lattice expansion and transformation rates of α and β phases in Ti–6Al–4V. *Mater. Sci. Eng. A* **391**, 104–113 (2005).
40. Yadroitsev, I., Krakhmalev, P., Yadroitsava, I., Johansson, S. & Smurov, I. Energy input effect on morphology and microstructure of selective laser melting single track from metallic powder. *J. Mater. Process. Technol.* **213**, 606–613 (2013).
41. Welsch, G., Boyer, R. & Collings, E. W. *Materials Properties Handbook: Titanium Alloys*. (ASM International, 1993).
42. Thijs, L., Verhaeghe, F., Craeghs, T., Humbeeck, J. Van & Kruth, J.-P. A study of the microstructural evolution during selective laser melting of Ti–6Al–4V. *Acta Mater.* **58**, 3303–3312 (2010).
43. Vrancken, B., Thijs, L., Kruth, J. P. & Van Humbeeck, J. Heat treatment of Ti6Al4V produced by Selective Laser Melting: Microstructure and mechanical properties. *J. Alloys*

Compd. **541**, 177–185 (2012).
44. Mulay, R. P., Moore, J. A., Florando, J. N., Barton, N. R. & Kumar, M. Microstructure and mechanical properties of Ti-6Al-4V: Mill-annealed versus direct metal laser melted alloys. *Mater. Sci. Eng. A* **666**, 43–47 (2016).
45. Voisin, T. *et al.* Defects-dictated tensile properties of selective laser melted Ti-6Al-4V. *Mater. Des.* **158**, 113–126 (2018).
46. Xu, W. *et al.* Additive manufacturing of strong and ductile Ti-6Al-4V by selective laser melting via in situ martensite decomposition. *Acta Mater.* **85**, 74–84 (2015).